Complex magnetic ordering in the oxide selenide $Sr_2Fe_3Se_2O_3$

Simon J Cassidy,[1] Fabio Orlandi,[2] Pascal Manuel,[2] Joke Hadermann,[3] Alex Scrimshire,[4] Paul A Bingham[4] and Simon J Clarke[1*]

[1]Department of Chemistry, University of Oxford, Inorganic Chemistry Laboratory, South Parks Road, Oxford, OX1 3QR, UK. [2]ISIS Facility, STFC Rutherford Appleton Laboratory, Harwell Oxford, Didcot OX11 0QX, United Kingdom. [3] Electron Microscopy for Materials Science (EMAT), University of Antwerp, Groenenborgerlaan 171, B-2020 Antwerp, Belgium., [4] Materials and Engineering Research Institute, Faculty of Arts, Computing, Engineering and Sciences, Sheffield Hallam University, City Campus, Howard Street, Sheffield, S1 1WB,UK.

*Corresponding author

email: simon.clarke@chem.ox.ac.uk

Abstract

$Sr_2Fe_3Se_2O_3$ is a localised-moment iron oxide selenide in which two unusual coordinations for Fe^{2+} ions form two sublattices in a 2:1 ratio. In the paramagnetic region at room temperature the compound adopts the crystal structure first reported for $Sr_2Co_3S_2O_3$, crystallising in space group *Pbam* with a = 7.8121 Å, b = 10.2375 Å, c = 3.9939 Å and Z = 2. The sublattice occupied by two thirds of the iron ions (Fe2 site) is formed by a network of distorted *mer*-[$FeSe_3O_3$] octahedra linked via shared Se_2 edges and O vertices forming layers, which connect to other layers by shared Se vertices. As shown by magnetometry, neutron powder diffraction and Mössbauer spectroscopy measurements, these moments undergo long range magnetic ordering below T_{N1} = 118 K, initially adopting a magnetic structure with a propagation vector (½–δ, 0, ½) ($0 \leq \delta \leq 0.1$) which is incommensurate with the nuclear structure and described in the *Pbam1'(a01/2)000s* magnetic superspace group, until at 92 K (T_{INC}) there is a first order lock-in transition to a structure in which these Fe2 moments form a magnetic structure with a propagation vector (½ , 0, ½) which may be modelled using a $2a \times b \times 2c$ expansion of the nuclear cell in space group 36.178 B_ab21m (BNS notation). Below T_{N2} = 52 K the remaining third of the Fe^{2+} moments (Fe1 site) which are in a compressed *trans*-[$FeSe_4O_2$] octahedral environment undergo long range ordering, as is evident from the magnetometry, the Mössbauer spectra and the appearance of new magnetic Bragg peaks in the neutron diffractograms. The ordering of the second set of moments on the Fe1 sites results in a slight re-orientation of the majority moments on the Fe2 sites. The magnetic structure at 1.5 K is described by a $2a \times 2b \times 2c$ expansion of the nuclear cell in space group 9.40 I_ab (BNS notation).

Introduction

Multi-anion compounds adopt a diverse range of structures and have received recent attention in several contexts. Oxide sulfides and oxide selenides enable band gap tuning for semiconductors and transparent conductors[1,2,3] and are of interest as potential thermoelectric materials.[4] Superconductors based on iron arsenides[5] and selenides[6] also often contain oxide, or hydroxide[7] slabs separating the iron arsenide or selenide layers. In oxide chalcogenides ordering of the oxide and heavier chalcogenide (S^{2-}, Se^{2-} or Te^{2-}) anions is the norm as a result of their differing sizes and chemistry.[8] Layered crystal structures often result, in which cations of main group and transition metals are separated according to their oxo- and chalcophilicity. Often, transition metal cations in oxide chalcogenides have coordination environments that contain both anions, e.g. in structures such as that of $La_2Fe_2Se_2O_3$[9] which has layers composed of face-sharing *trans*-$FeSe_4O_2$ octahedra separated by PbO-type LaO layers. Sometimes the resulting structures are less obviously layered, but maintain some low-dimensional feature of the magnetic exchange interactions which results in unusual phenomena such as in $SrFe_2Se_2O$, which contains $FeSe_2O_2$ tetrahedra that link to form what has been described as a spin-ladder with multiple competing exchange interactions.[10] Some multi-anion coordination environments are inherently polarised such as those in CaFeSeO[11,12,13] and CaFeSO[14] which contain all-vertex-linked $FeSe_2O_2$ and S-vertex-linked FeS_3O tetrahedra respectively, and which crystallise in different structures, both with non-centrosymmetric space groups (CaFeSeO also has a centrosymmetric polymorph).[11] The oxide selenide $Sr_2Fe_3Se_2O_3$ has recently been reported by Lai *et al.*,[15] along with the sulfide analogues for both Fe[15] and Co,[16] in work which has been carried out independently of our own. In $Sr_2Fe_3Se_2O_3$ and $Sr_2Fe_3S_2O_3$[15] a new coordination environment for Fe^{2+} is described and there are a succession of magnetic phase transitions on cooling to a state in which all the Fe^{2+} ions are participating in magnetic long range order. Here we use neutron powder diffraction (NPD) and Mössbauer spectroscopy to probe the magnetic ordering as a function of temperature and correlate the behaviour with the detailed analysis of magnetometry and Mössbauer data made by Lai *et al.*[15]

Experimental

Synthesis.

Polycrystalline samples of $Sr_2Fe_3Se_2O_3$ were synthesised from stoichiometric amounts of SrO, FeSe, Fe_2O_3 (Alfa Aesar 99.998 %) and Fe (Alfa Aesar 99.998 %). The SrO was prepared by thermal decomposition of $SrCO_3$ (Alfa Aesar 99.997 %) under dynamic vacuum for 16 hours at 800 °C followed by 4 hours at 1100 °C. FeSe was prepared by stoichiometric reaction of iron (Alfa Aesar 99.998 %) and selenium (Alfa Aesar 99.999 %) powders at 700 °C for 48 hours. The four reactants were ground together inside an argon-filled dry glovebox (Glovebox Technology Ltd, UK) using an agate pestle and mortar. The ground powder was pressed into a pellet, placed inside an alumina crucible, and sealed inside an evacuated silica ampoule. Various heating protocols were then investigated as described in the results section.

Diffraction Measurements.

Laboratory X-ray powder diffraction (XRPD) measurements to monitor phase purity and the course of the reactions were performed on a Panalytical Empyrean diffractometer using Cu$K_{\alpha 1}$ radiation. High resolution XRPD measurements for structure solution and analysis were performed on beamline I11[17] at the Diamond Light Source, Ltd, UK, and additional measurements were made on beamline ID22 at the European Synchrotron Radiation Facility (ESRF), France. NPD measurements were performed from 10 – 300 K on the WISH instrument[18] at the ISIS Pulsed Neutron and Muon Facility, UK with the samples contained in indium-sealed thin-walled vanadium cylinders. Structure solution and Rietveld refinements were performed using the TOPAS Academic software.[19] Electron diffraction measurements at EMAT, Antwerp, were acquired with a Philips CM20 transmission electron microscope operated at 200 kV with the sample prepared by grinding the crushed powder in ethanol and depositing a few drops of the suspension on holey carbon TEM grids.

Magnetometry.

All measurements used a Quantum Design MPMS-XL SQUID magnetometer. The susceptibility was determined by measuring the magnetisation as a function of temperature on warming from 2 to 300 K after cooling both in a zero applied field: zero-field-cooled (ZFC) and in the measuring field: field-cooled (FC) of 50 mT. Magnetisation isotherms ($-5 \leq \mu_0 H/\mathrm{T} \leq +5$) at several temperatures were each measured after cooling the sample from 200 K (i.e. well above the highest magnetic ordering transition) to the measurement temperature in a +5 T field and then measuring the magnetisation while sweeping the field in steps down to –5 T and back to +5T. Successive isotherms were collected from highest to lowest temperature. Between the measurement of successive isotherms, the field was changed to 0T and the sample warmed to 200 K, then the field was changed to +5 T prior to cooling. This was in an attempt to remove any influence of the previous measurement on the next. Samples were sequestered from air in gelatin capsules.

Mössbauer Spectroscopy.

^{57}Fe Mössbauer spectra were collected using a constant-acceleration, cryostatic spectrometer (Janis 10 K CCR, model CCS-800/204N) with a Lakeshore 335 temperature controller. The radiation source

^{57}Co(Rh) was kept at room temperature. A Mössbauer thickness of 1[20] was achieved by homogenously mixing 25 mg of $Sr_2Fe_3Se_2O_3$ with graphite to fully pack a cylindrical cavity (1.77 cm^2 cross-section, 0.1 cm thick) in an acrylic disc, which was sealed air-tight. Spectra were analysed using the *Recoil* software package[21] to deconvolve the data into separate iron environments. Extracted chemical shift values are quoted relative to a thin α-Fe foil calibration.

Results and Discussion

Synthesis.

A preliminary synthesis using only SrO and FeSe in equimolar quantities was found to produce the reported phase with a large proportion of SrSe impurity. The synthesis was then modified by the inclusion of Fe_2O_3 and Fe to target $(FeO)_x(SrSe)_y$ compositions with $x > y$ to minimise impurities and infer the composition. Sample purity and Bragg peak asymmetry were found to vary greatly with the synthesis temperature, even with the correct compositional ratio of elements. Common impurities included SrSe, Fe_3O_4, $SrFe_2Se_2O$, and FeO. Repeated annealing at 760 °C or below yielded a composition with higher levels of FeO or Fe_3O_4 impurity (~2-5 % by mass), whereas repeated annealing above 760 °C yielded a product with higher levels of $SrFe_2Se_2O$ impurity (3-8 % by mass). The highest purity samples were produced by placing the sealed crucible into a preheated furnace at 900 °C and leaving it to dwell for only 80 minutes before quenching in ice water. This is similar to the bulk synthesis reported by Lai *et al.*, although their reaction was of a longer duration. This method produced samples with ~1.1 % SrSe, 1.6 % $SrFe_2Se_2O$, and 0.3 % FeO by mass (sample ***A***). The product was a grey powder and the room temperature resistivity of a cold-pressed pellet of sample ***A*** was measured as 0.4 MΩcm, suggesting insulating behaviour. A second sample made by repeated annealing at 740°C in the intentionally slightly SrSe-rich stoichiometric ratio of 7Sr:10Fe:7Se:10O has also been used in this work (sample ***B***), which contained only 0.9% $SrFe_2Se_2O$ and 1.2% FeO as well as a 5.6% SrSe impurity, which was readily treated as a second phase in the Rietveld refinement.

Structure solution.

The laboratory XRPD pattern of $Sr_2Fe_3Se_2O_3$ was initially indexed on an orthorhombic unit cell with dimensions of 7.81 × 10.23 × 3.99 Å. Electron diffraction patterns on sample ***B*** confirmed the same unit cell and showed reflection conditions: $0kl : k = 2n$, $h0l : h = 2n$, $h00 : h = 2n$, $0k0 : k = 2n$, corresponding to the extinction coefficient *Pba-*, allowing space groups *Pba*2 and *Pbam*. These diffractograms (Figure 1) showed well-formed spots with no evidence for streaking in the regions investigated. Structural solution was performed using charge flipping, as implemented in *TOPAS*

Academic,[21] with *Pbam* symmetry imposed, using high resolution PXRD data collected with the I11 instrument. The algorithm was successful in identifying the locations of all ions in the unit cell, allowing the identity of the ions on each site to be subsequently deduced by comparison of their inter-ionic distances with those in relevant binary compounds.

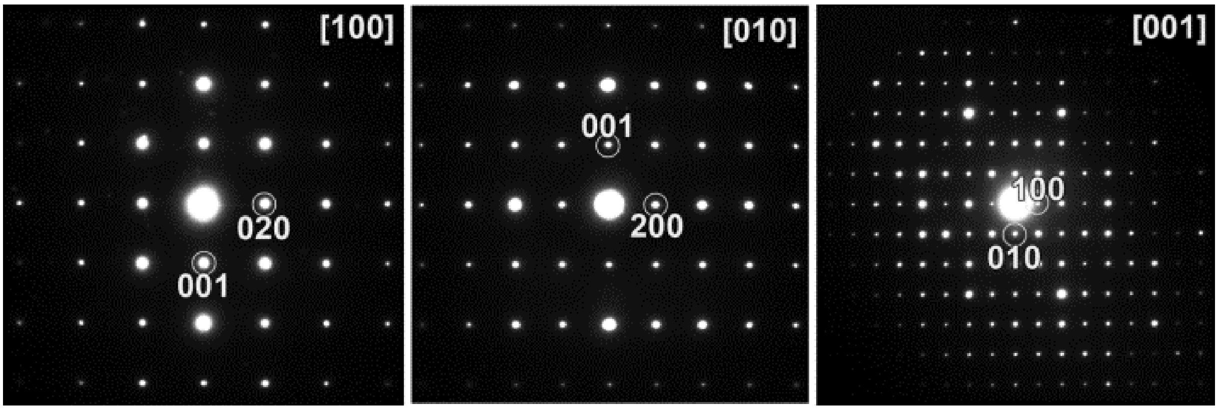

Figure 1. Electron diffractograms of $Sr_2Fe_3Se_2O_3$ along the major zone axes.

The structural model obtained from charge-flipping was confirmed and refined using Rietveld analysis. At this stage, the model was trialled in space group *Pba*2; the other candidate space group that accounted for the systematic absences in the electron diffraction experiment. In reducing the symmetry from *Pbam* to *Pba*2, site positions are allowed to refine freely along the *z* axis – a consequence of the lack of the centre of inversion. No significant improvement to the fit or change in the atomic positions was observed on allowing this reduction of symmetry and so centrosymmetric *Pbam* was chosen as the space group. During the course of our work we became aware of the discovery of the isostructural compound $Sr_2Co_3S_2O_3$[16] and the report of $Sr_2Fe_3\mathit{Ch}_2O_3$ (*Ch* = S, Se)[15] in which single crystal X-ray diffraction confirmed this choice of space group *Pbam.* Rietveld refinement against synchrotron powder X-ray diffraction acquired using I11 achieved a good agreement to the data for sample ***B*** shown in Figure 2 and sample ***A*** shown in Figure S1. The result of the structural analysis (Table 1) is entirely consistent with the report of Lai *et al.*[15]

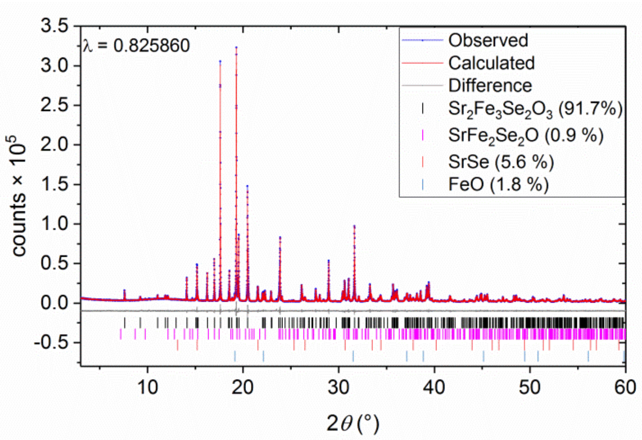

Figure 2 Rietveld refinement against the PXRD pattern (I11) of $Sr_2Fe_3Se_2O_3$ sample ***B*** taken at room temperature (note that this sample was intentionally prepared with a slight excess of SrSe in the reaction mixture, hence the presence of significant amounts of this phase in the sample).

The $Sr_2Fe_3Se_2O_3$ structure is shown in Figure 3. For further discussion of the structure the reader is also referred to the works of Lai *et al.*[15,16] The key features of the structure are as follows: there are two iron coordination environments shown in Figure 3(a): Fe1 has a compressed *trans*-$FeSe_4O_2$ octahedral environment with a multiplicity of 2 in the unit cell, while Fe2 has a distorted *mer*-$FeSe_3O_3$ octahedral environment with a multiplicity of 4 in the unit cell. The two environments have complex interconnectivity shown in Figure 3(b): each *trans*-$FeSe_4O_2$ octahedron (Fe1) shares four faces (necessarily Se_2O_1) with *mer*-$FeSe_3O_3$ octahedra (Fe2), and is linked to two other *trans*-$FeSe_4O_2$ (Fe1) octahedra through Se_2 edges to form chains of the *trans*-$FeSe_4O_2$ (Fe1) polyhedra extending along the *c* axis. *Mer*-$FeSe_3O_3$ octahedra (Fe2) connect to each other via Se_2 edges which are the same as those shared to form the chains of *trans*-$FeSe_4O_2$ (Fe1) octahedra extending along *c* (Figure 3(b). The *mer*-$FeSe_3O_3$ (Fe2) octahedra are further linked along the *c* direction though *trans* O vertexes to two other *mer*-$FeSe_3O_3$ octahedra (Fe2). Lai *et al.*[15,16] describe this motif (Figure 3(b)) extending along the *c* axis as a necklace ladder. The remaining O vertexes of the *mer*-$FeSe_3O_3$ (Fe2) octahedra join these necklace ladders along the *a* direction and the resulting double chains of O-vertex-linked *mer*-$FeSe_3O_3$ (Fe2) octahedra which extend along *c* are described as a 2-leg rectangular ladder.[16] These connected ladders form a layer as shown by the solid bonds in Figure 3(c) that Lai *et al.* describe as a hybrid spin ladder.[15,16] These hybrid ladders are joined together along the *b* axis by sharing of the remaining Se vertexes of the *mer*-$FeSe_3O_3$ (Fe2) octahedra as indicated by the dotted bonds in Figure 3(c).

The coordination environments found in this compound should be compared with other transition metal oxide chalcogenides. The *trans*-$FeSe_4O_2$ coordination is found in $La_2Fe_2Se_2O_3$[9] and relatives such as $Sr_2Fe_2Se_2OF_2$,[22] $Na_2Fe_2Se_2O$,[23] and the phase of $BaFe_2Se_2O$ synthesised at high pressure,[24] in which the polyhedra share faces producing layers containing Fe_2O sheets, an arrangement also found in chalcogenide and pnictide analogues with these structure types containing other transition metals[25,26,27,28] and in the structurally related oxide sulfide $Ca_2Fe_{2.6}S_2O_3$.[29] Both polymorphs of $La_2FeSe_2O_2$ also display this coordination environment for Fe^{2+} ions with linking via shared selenide edges,[30] and this coordination environment and mode of connection is also found in $La_5V_3O_7S_6$.[31] As discussed by Lai *et al.* in the original report of $Sr_2Co_3S_2O_3$[16] the *mer*-[MX_3O_3] octahedral environment (M = transition metal; X = non-oxide ion) is rare, although it has been reported for TiS_3O_3 octahedra in $La_6Ti_2S_8O_5$.[32]

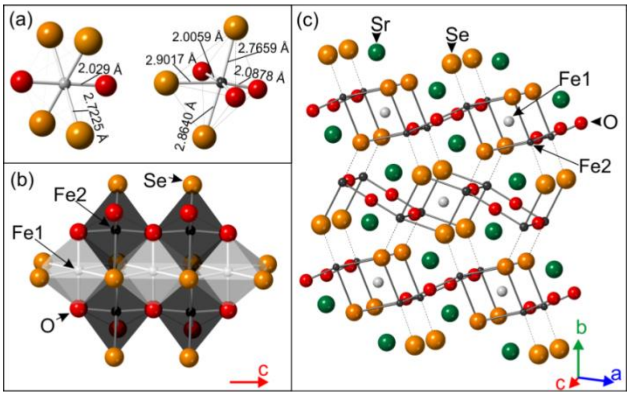

Figure 3. (a) the local coordination enviroments of the two iron sites; (b) connectivity of the Fe1 and Fe2 octahedra, described by Lai *et al.* as the necklace ladder; (c) Structure of $Sr_2Fe_3Se_2O_3$ showing the Fe2 bonding network. Solid bonds show linkages of Fe2 in the necklace ladder and 2-leg ladder that together form a layer described as a hybrid spin ladder,[15,16] which joins to adjacent ladders through selenide vertexes (dashed bonds).

Magnetometry.

Our magnetic susceptibility measurements show transitions consistent with those observed using magnetometry and heat capacity measurements by Lai *et al.*[15] In what follows we adopt their notation. The transitions are shown in Figure 4(b) at ~125 K (T_{N1}), 50 K (T_{N2}) and 40 K (T'). T_{N1} coincides approximately with the Verwey transition of Fe_3O_4, and while only 0.05 % of this phase (below the detection limit of bulk diffraction measurements) would be required to produce such a transition in the magnetisation, the heat capacity measurements of Lai *et al.*[15] show that this feature is associated with the bulk of the sample. Figure 4(a) shows a change in the shape of the hysteresis loops, obtained after field-cooling from room temperature at 5 T, on passing through the 50 K (T_{N2}) and 40 K (T') transitions. Below T' a metamagnetic transition appears at about 0.6 T in the magnetisation isotherm. This feature persists to lower temperatures and is evident in the virgin curve of the magnetisation isotherm at 2 K obtained after zero-field-cooling in the report of Lai *et al.*[15] In our field-cooled (5 T) isotherm at 2 K a higher-field feature is evident above 2 T which was also observed in the hysteresis loop of Lai *et al.*[15] The behaviour suggests that there may be a field-dependence to the magnetic ordering which would require neutron diffraction investigations beyond the scope of those performed here.

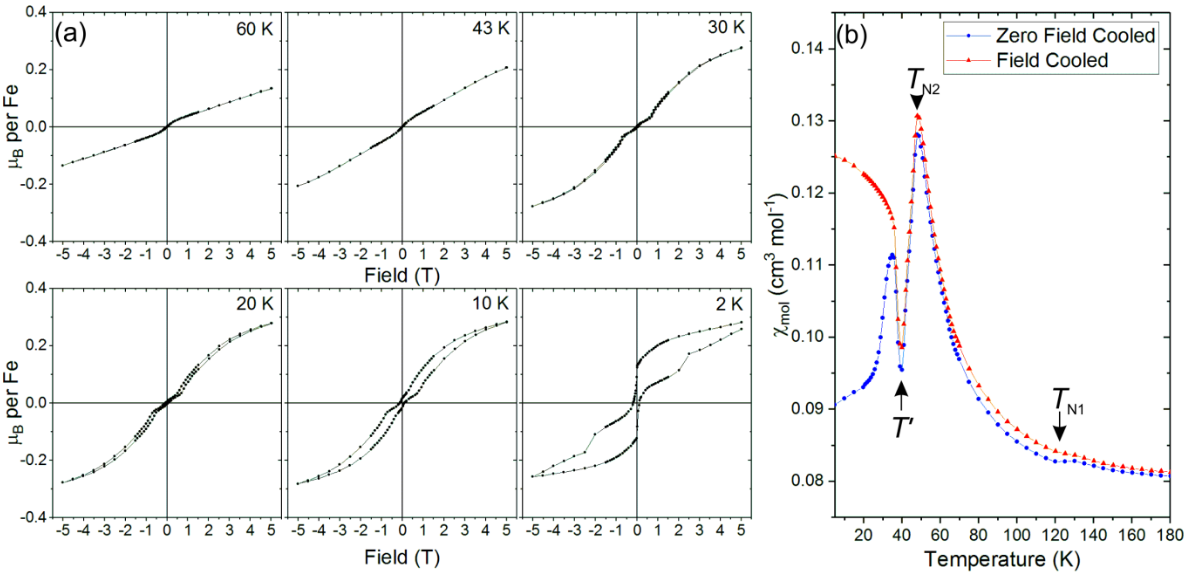

Figure 4 (a) Magnetisation isotherms measured by cooling sample *B* from 200 K in a +5T field to the measurement temperature and sweeping the field to –5 T and back to +5T. (b) Zero-field-cooled and field-cooled temperature dependence of the magnetic susceptibility of sample ***B*** measured in a 1000 Oe field.

Neutron Powder Diffraction.

Variable temperature NPD measurements (Figure 5) were carried out on both sample ***A*** and sample ***B*** on warming. Sample ***A*** was measured in narrow temperature steps from 1.5 K to 150 K, while diffraction patterns with better statistics were collected on sample ***B*** at 20, 55, 97, and 135 K corresponding to key ordered states. Rietveld refinements against data from both samples produced identical models for the magnetic ordering. On cooling we observe magnetic ordering transitions as follows. Below 118 K (equated with T_{N1}) magnetic Bragg peaks begin to appear. On cooling further these peaks shift remarkably in *d*-spacing until 92 K is reached (Figure 5). We identify this temperature as a fourth magnetic transition for this compound which is not evident in the magnetic susceptibility measurements. We give this the symbol T_{INC} because it is associated with the transition between commensurate and incommensurate magnetic ordering as described below. Below 51 K (T_{N2}) an additional set of magnetic reflection appears, which increase sharply in intensity as the temperature is lowered, as can be seen in the change in intensity of the peak at 3.8 Å between 48 and 42 K in Figure 5..

Analysis of the commensurate reflections was performed using the ISODISTORT software,[33] coupled with Rietveld refinement in Topas Academic v6.[19] Rietveld refinement of the incommensurate magnetic structure was performed using FullProf.[34]

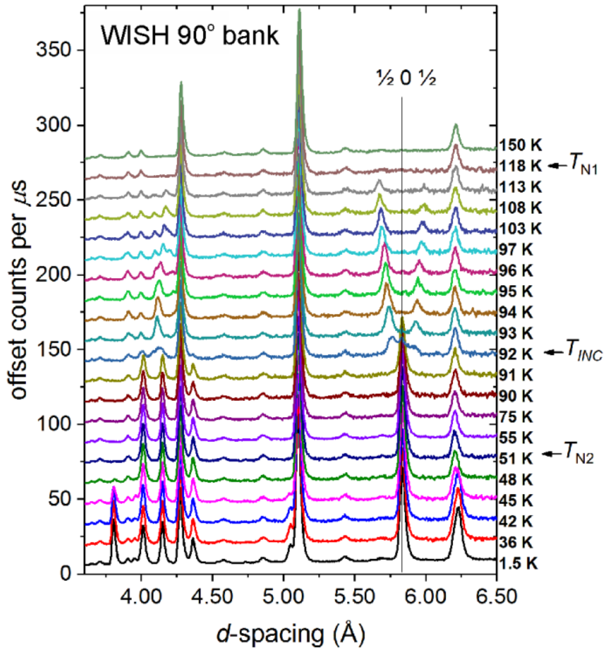

Figure 5. Evolution with temperature of the neutron powder diffraction patterns of $Sr_2Fe_3Se_2O_3$ sample ***A*** measured as a function of temperature. Data from the detector bank with a mean 2θ of 90° are shown.

Magnetic scattering in all diffraction patterns above T_{N2} = 51 K could be accounted for solely by ordering on one of the Fe sites. In principle the magnetic contribution to the Bragg scattering alone does not allow us to distinguish whether the Fe1 or the Fe2 site is responsible. However the Fe2:Fe1 ratio of 2:1 enabled us to deduce, from the size of the ordered moment, that the Fe2 site (the *mer*-$FeSe_3O_3$ site which accounts for two thirds of the iron sites) must be the one ordered in this regime (with an ordered moment of 3.04(1) μ_B at 55 K) otherwise the less numerous Fe1 sites would each carry an ordered moment of 4.75(2) μ_B at 55 K, which exceeds the maximum saturated value expected for Fe^{2+}. This result is consistent with the Mössbauer data (see below). We firstly consider the magnetic structure that pertains between T_{N2} (51 K) and T_{INC} (92 K). This can be accounted for (Figure 6 shows the refinement against 55 K data) by commensurate ordering of the Fe2 moments with propagation vector *k* = (½, 0, ½). Trials of the possible magnetic ordering modes in the expanded unit cell gave a good fit to the data with a combination of $mU_2(\xi_1,0)$ modes (following the notation[35,36] of Miller and Love used in ISODISTORT). This may be described in the magnetic space group B_ab2_1m (36.178) (BNS notation).[37] The ordering scheme is as shown in Figure 7, in which the moments are directed along the *c* axis with antiferromagnetic coupling (J_1). In the direction of the *a* axis, the moments are antiferromagnetically aligned along the vertex-sharing 180° Fe(2)–O–Fe(2) pathways (J_2), and ferromagnetically aligned along the 99° Fe(2)–Se–Fe(2) pathways (J_3) resulting from edge sharing. These three J_1 couplings in the *ac* plane occur in the hybrid spin ladders described by Lai *et al.*[15] It is these intra-ladder interactions that appear to dominate the magnetic ordering scheme between T_{N2} and T_{INC}. The alignment of spins by the inter-ladder couplings (J_4-J_7) exhibits an inherent frustration: according to the refined magnetic structure, for half the Fe2 ions J_4 is ferromagnetic but J_5, J_6 and J_7 are antiferromagnetic and for the other half of the Fe2 ions J_4 is antiferromagnetic but J_5, J_6 and J_7 are ferromagnetic. The ordering is summarised in the schematic in Figure 7(d).

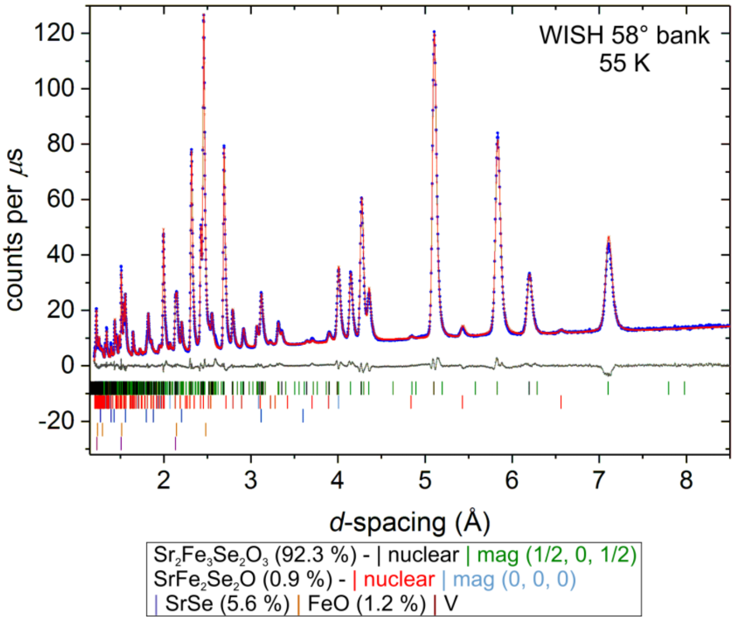

Figure 6. Rietveld refinement against NPD data collected with sample ***B*** at 55 K (i.e. between T_{N2} and T_{INC} with commensurate antiferromagnetic ordering on the Fe2 sites). Data from the detector bank with a mean 2θ of 58° are shown.

We note that the resulting magnetic space group is polar, indicating that the magnetic transition at T_{INC} breaks the spatial inversion symmetry. Indeed, the magnetic order, which transforms as the $mU_2(\xi_1,0)$ irreducible representation, couples a displacive distortion with the $\Gamma_4^-(\sigma)$ symmetry through the linear quadratic invariant $\sigma\xi_1^2$ in the free energy. This lattice distortion can give rise to a net dipolar moment in the structure and it is probably the origin of the frustration release in the inter-ladder couplings (J_4–J_7 in Figure 7).

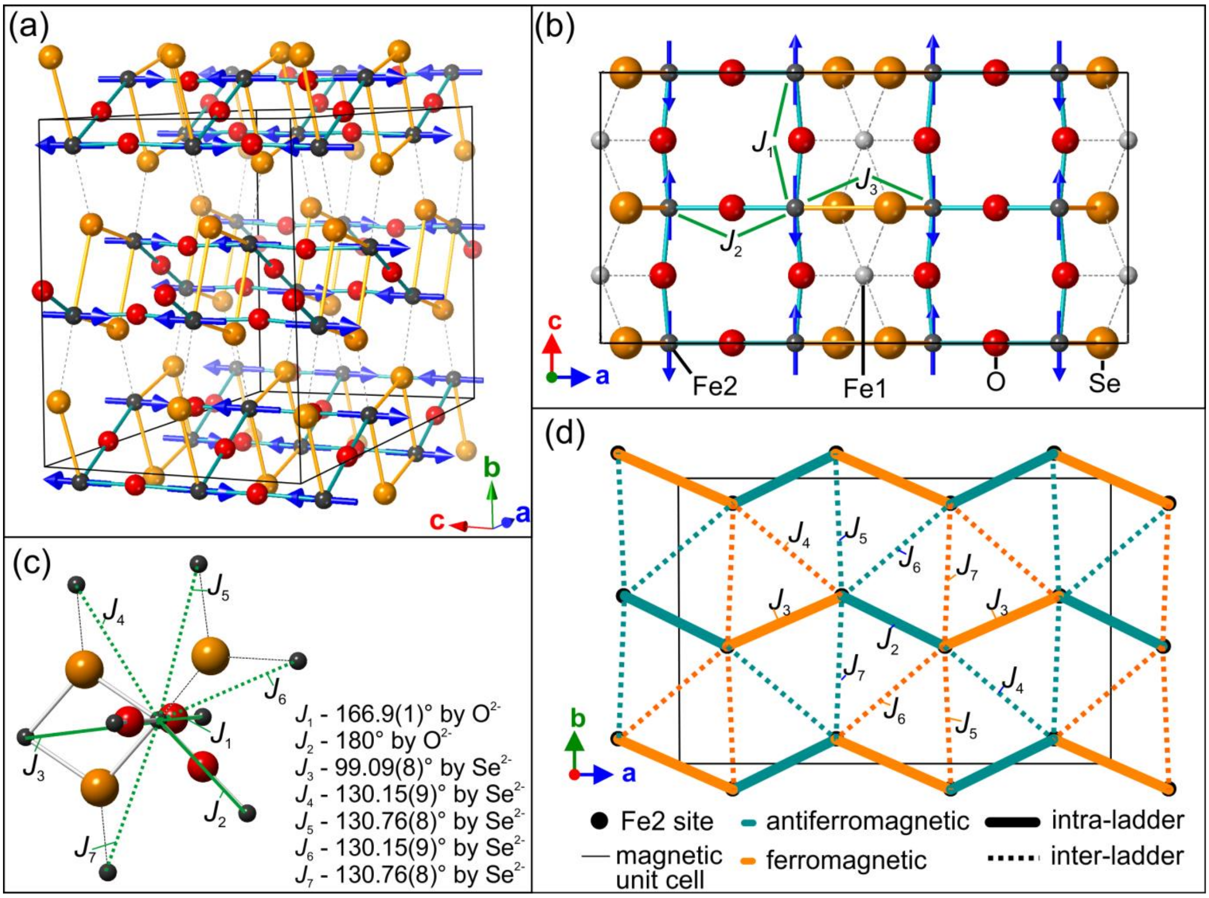

Figure 7 (a) Magnetic ordering scheme of the Fe2 sites between 51 (T_{N2}) and 92 K (T_{INC}) consisting of moments pointed along the *c* axis. Sr and Fe1 sites are not shown. (b) Arrangement of the Fe2 magnetic moments in the hybrid spin ladder. (c) Local environment of an Fe2 ion with *J*-couplings to seven other Fe2 ions that are mediated by a single anion: three of which are intra-ladder and four are inter-ladder (d) schematic diagram of the magnetic ordering and couplings with colours indicating the relationships between neighbouring spins. The magnetic moments in the diagram are directed in the plane along the *c* axis and are coupled antiferromagnetically (J_1) down that axis on all Fe2 sites. The unit cell shown is that of the magnetic cell, doubled along the *a* and *c* axes relative to the nuclear cell.

On warming through T_{INC} the magnetic Bragg peaks on a propagation vector (½, 0, ½) develop satellite peaks which can be indexed to a propagation vector of (½–δ, 0, ½) ($0 \leq \delta \leq 0.1$). The transition appears sharp and first order, with solely commensurate ordering observed at 91 K, coexistence of the commensurate and incommensurate phases observed at 92 K (shown in the supporting information Figure S2), and solely incommensurate ordering observed at 93 K. The satellite peaks diverge from the commensurate ordering vector above 93 K as shown for the ½ 0 ½ reflection in Figure 5, appearing at positions ½±δ 0 ½ with δ increasing from 0 to a maximum of 0.10

before long range order is lost at T_{N1}. Our model for the incommensurate magnetic structure is still described by spins directed along the *c* axis, with antiferromagnetic alignment (J_1). Magnetic couplings in the *a* axis still have net antiferromagnetic alignment along the 180° oxide linkages (J_2) and net ferromagnetic alignment along the 99° selenide linkages (J_3) however, there is a modulation in the size of the ordered moment along *a* as shown in Figure 8. The occurrence of this incommensurate magnetic structure is presumably a response to the inherent frustration of the interlayer interactions (J_4-J_7) in the commensurate structure below T_{INC}, shown by the dotted lines in Figure 7(c): the modulation in each layer is out of phase with that in the adjacent layer, such that when the moment is at a maximum in one layer it is at a minimum in the layer below. Numerous systems are known where frustration of magnetic interactions results in the adoption of a modulated magnetic structure.[38,39,40,41] Attempts to model the magnetic scattering using a cycloidal magnetic structure produced poor fits (see Figure S8).

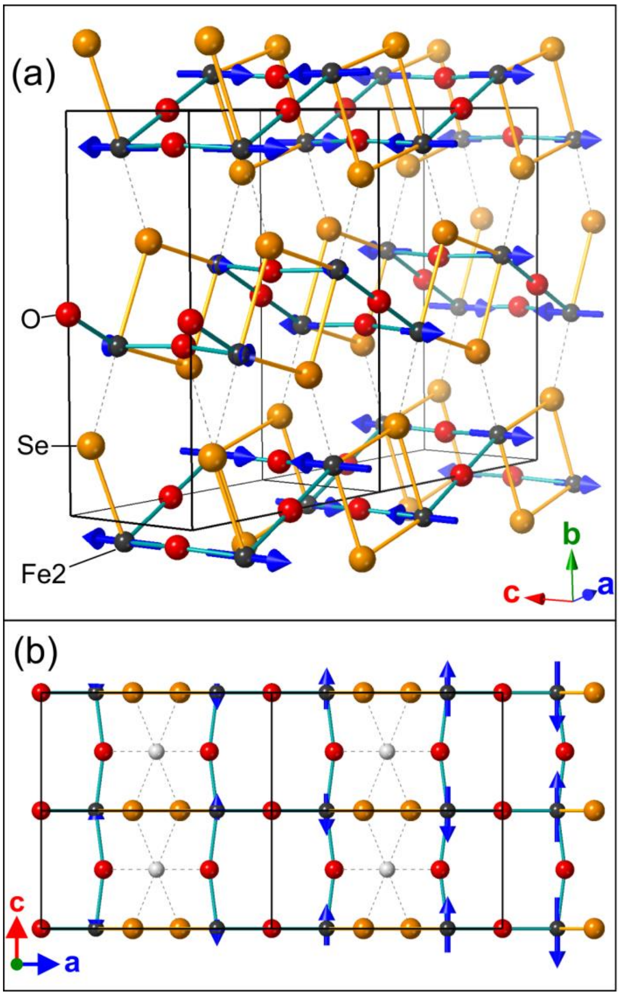

Figure 8 (a) Magnetic ordering scheme of the Fe2 sites between 120 (T_{N1}) and 92 K (T_{INC}) consisting of moments pointed along the *c* axis and an spin density wave incommensurate with the crystal structure in the *a* axis (propagation vector (*α*, 0, ½) with *α* = 0.42 in the case shown). (b) Arrangement of the Fe2 magnetic moments in the hybrid spin ladder. The unit cell shown is the

nuclear cell. Fe1 sites are not shown in (a) and Sr sites are not shown in (a) or (b). See caption to Figure 7 for the convention on coloring of bonds.

Rietveld refinement against the neutron diffraction pattern at 96 K is shown in Figure 9(a). The incommensurate magnetic structure is described within the *Pbam*1’(*a*0½)000*s* superspace group corresponding to the action of the mA3 irreducible representation of the parent space group and can be described as a spin density wave with amplitude ~3.0 μ_B at 95 K. The transition at T_{INC} is a lock-in on cooling from the incommensurate propagation vector to the commensurate (½ 0 ½) value with a locking of the origin (corresponding to a locking of the phase of the sine wave) along the propagation vector direction to the value 1/8+*n*/2, where *n* is an integer number, resulting in the B_ab2_1m magnetic space group. There appears to be no discernable signature of this transition in the susceptibility measurements.

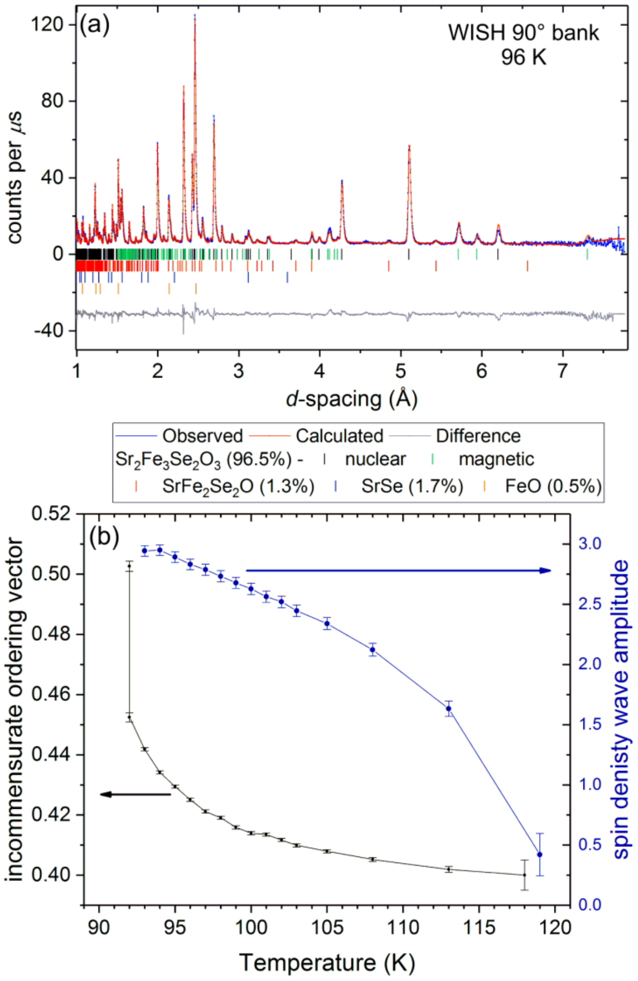

Figure 9. Rietveld refinement against WISH NPD data (data bank with a mean 2θ of 90°) of sample ***A*** at 96 K where the magnetic structure is incommensurate with the crystal structure (propagation vector (*a*, 0, ½) with *a* = 0.42 in the case shown). (b) Plot of the amplitude of the spin density wave of

the Fe2 sites and of the variable component *a* of the propagation vector (*a*, 0, ½) against temperature.

A second set of magnetic reflections appears below T_{N2} (51 K), which index on a propagation vector *k* = (½, ½, 0). These arise from the long range ordering of the moments on the Fe1 sites combined with the existing magnetic ordering of the Fe2 sites, this gives an overall magnetic unit cell of $2a \times 2b \times 2c$ relative to the structural cell. ISODISTORT was used to test ordering schemes for the Fe1 moments that might contribute to the additional reflections observed below T_{N2}, with *k* point S (*k*=½, ½, 0), for which it was found the majority of the new magnetic scattering could be accounted for by a combination of mS3+S4+(ε_1,ε_2) modes, however it was not possible to fit the new magnetic intensities (Figure 10) which occur below T_{N2} using solely a combination of the Fe1 magnetic ordering modes without serious discrepancies. Allowing the already-ordered Fe2 moments to reorient so that they would contribute to the intensity of these new magnetic Bragg peaks that emerge below T_{N2} gave a much improved fit, with better visual agreement and a lowered R_{wp} from 7.8 to 4.6 %. In the overall fit the Fe1 moments lie along the Fe1–O bonds in the *ab* plane, which was also the conclusion of Lai *et al.*[15] from fitting of their Mössbauer data, and this and their ferromagnetic alignment via sharing of Se_2 edges is consistent with the orientation of moments in the magnetic structure of $Sr_2Fe_2S_2OF_2$.[42] The Fe2 moments that were already ordered above T_{N2} remain principally directed along the *c* axis with the mU2 ordering scheme, however to fully account for the magnetic intensities below T_{N2} they acquire a canting in the *ab* plane described by a combination of mS3+S4+ modes. A comparison of the fit with and without this Fe2 site canting is given in the supporting information (Figure S3). This rearrangement of the spins becomes established at 40 K and may be associated with the *T'* transition in heat capacity measurements of Lai *et al.*[15] The canting puts the Fe2 moments in a plane with their nearest Fe1–O bond and the corresponding Fe1 moment, with antiferromagnetic alignment between each of the Fe1 moments and the Fe2 moments canting as shown in Figure 11(a). The ordering scheme thus derived is purely antiferromagnetic, and can be described in the $I_{a}b$ magnetic space group in a $2a_{nucl} \times 2b_{nucl} \times 2c_{nucl}$ cell (Table S6). In light of the weak ferromagnetic component of the susceptibility evident in the magnetometry below *T′* at 40 K, ordering modes which gave a net ferromagnetic canting of one or both sets of spins were attempted but none gave improvement to the fit, suggesting that the zero-field magnetic structure (i.e. as measured in the NPD experiment) is purely antiferromagnetic. Moreover the determined magnetic space group does not allow any ferromagnetic moment in any crystallographic direction. Indeed, the magnetisation versus field curves shown in Figure 4 are close to linear at low fields, which is consistent with AFM ordering without an applied field.

To explain the canting of the Fe2 sublattice with the mS3+S4+(ε_1,ε_2) modes it is necessary to take into consideration a nuclear distortion with the right symmetry to allow a trilinear invariant in the free energy, coupling the two magnetic distortions. To conserve the translational symmetry of the parent structure, the nuclear distortion needs to have a propagation vector *q*=(0 ½ ½), the T point of the first Brillouin zone, and to transform as the T2 irreducible representation with order parameter direction P(δ_1,δ_2). This allows us to derive a trilinear invariant $a\xi_1(\varepsilon_1\delta_1 + \varepsilon_2\delta_2) + b\xi_1(\varepsilon_1\delta_2 - \varepsilon_2\delta_1)$ describing the coupling, mediated by the T2(δ_1,δ_2), between the magnetic mU$_2$(ξ_1,0) and mS3+S4+(ε_1,ε_2) distortions. Any monoclinic nuclear distortion was outside the resolution of the WISH diffractometer, and we did not observe any superstructure reflections consistent with *q*= (0 ½ ½). We used the X-ray diffractometer ID22 at the ESRF to investigate whether the magnetic ordering at T_{N2} gives rise to a small monoclinic distortion of the nuclear cell or the presence of 0 ½ ½ peaks, that might be associated with the *T'* transition in the heat capacity data of Lai *et al.*[15] Our measurement at 5K showed no apparent symmetry lowering distortion (Figure S4), but a careful observation of the diffraction pattern indicated the presence of a very weak reflection, not present at ambient temperatures, that could be indexed as the 0 5/2 ½ reflection (Figure S5). Even if this reflection is statistically significant, its spurious nature cannot be excluded, but its position and the propagation vector are consistent with the symmetry analysis. A refinement with the distorted monoclinic symmetry *Im* is not possible due to the weak character of the distortion (i.e. the low intensity of the proposed 0 5/2 ½ reflection) and the high number of free parameters. Even considering this extra nuclear distortion, on the ground state magnetic space group, the weak ferromagnetic moment is still not allowed from the resulting symmetry. Note that we needed to use an attenuated beam on ID22 to avoid sample heating when performing this experiment: with the full intensity beam sample heating was evident as had been observed and described in measurements down to 75 K by Lai *et al.* on the same instrument (see their Figure S4).[15] Figure 12 summarises the evolution of the ordered moments over the entire temperature range.

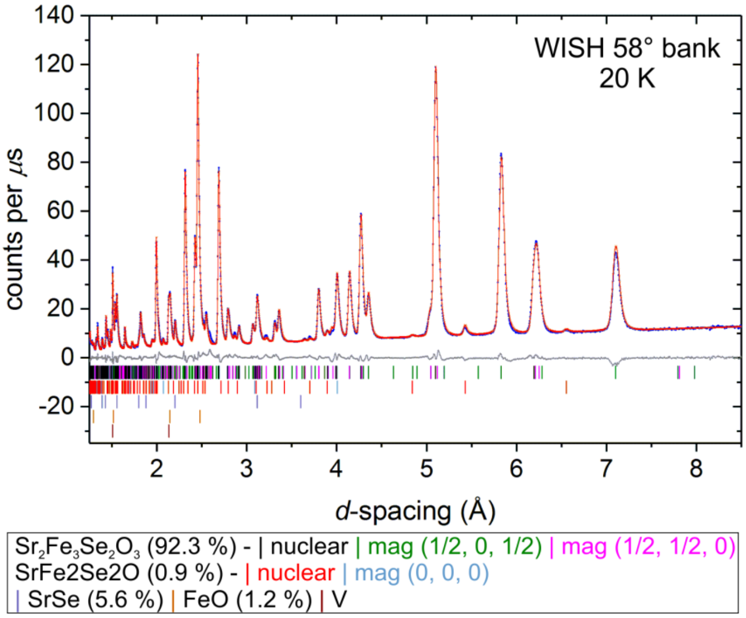

Figure 10. Rietveld refinement against NPD data collected with sample ***B*** at 20 K (below T_{N2} with both Fe sublattices ordered). Data from the detector bank with a mean 2θ of 58° are shown.

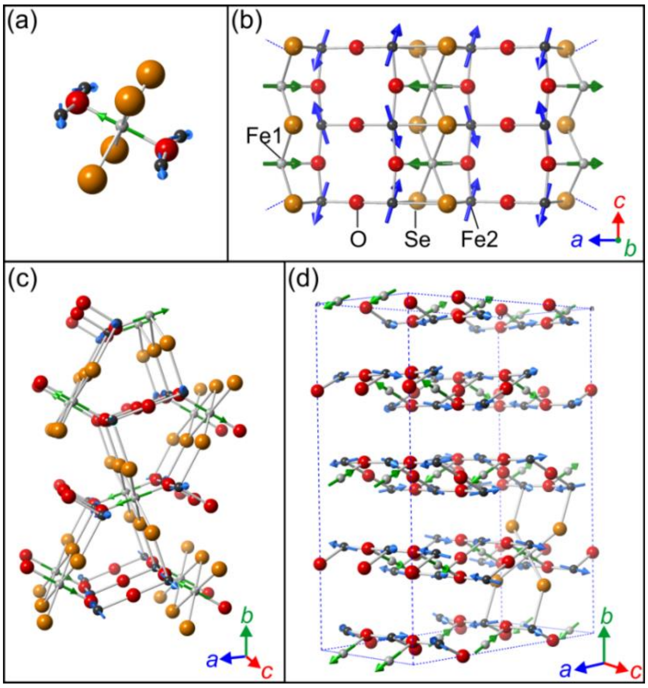

Figure 11. Magnetic structure of $Sr_2Fe_3Se_2O_3$ observed between 1.5 and 50 K (T_{N2}). (a) the local environment of the Fe1 moment relative to the nearest neighbour Fe2 sites. (b) Arrangment of Fe1 and Fe2 moments in the spin hybrid ladders (compare with Figure 7(b)). (c) Arrangment of moments between ladders. (d) magnetic unit cell below T_{N2}, which is a $2a \times 2b \times 2c$ expansion relative to the nuclear cell (see Table S6). Sr and most Se sites not shown in (d) for clarity.

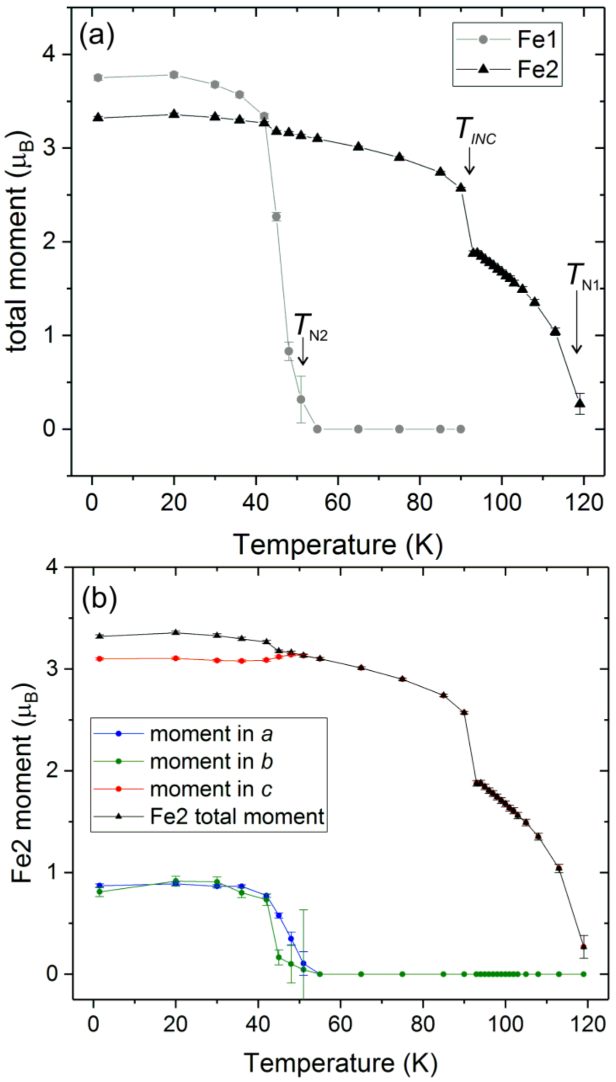

Figure 12. Evolution of (a) the total ordered moments on the two Fe sites and (b) the evolution of the components of the Fe2 moments showing the change in orientation that coincides with the onset of long range ordering of the Fe1 moments at T_{N2}. The kink in the magnitude of the Fe2 moment at T_{INC} is consistent with the first order character of the lock-in transition.

Table 1 Structural and magnetic information from Rietveld refinement of $Sr_2Fe_3Se_2O_3$. Further details are given in the supporting information.

Sample	$Sr_2Fe_3Se_2O_3$ sample ***B***			
Instrument	I11	WISH		
T (K)	298	135	55	20
Nuclear symmetry	*Pbam* (55)	*Pbam* (55)	*Pbam* (55)	*Pbam* (55)
a (Å)	7.8121(2)	7.8003(2)	7.7963(2)	7.7945(2)
b (Å)	10.23747(9)	10.2112(3)	10.2008(3)	10.1979(3)
c (Å)	3.99388(5)	3.99121(9)	3.98951(9)	3.9893(1)
V ($Å^3$)	319.413(7)	317.97(1)	317.18(1)	317.10(1)
Density (g cm^{-3})	5.70486(9)	5.7308(2)	5.7452(2)	5.7465(3)
R_{wp} (%)	5.22	4.10	4.55	4.61
χ^2	1.56	1.06	1.17	1.21
Sr–O × 2 × 1 × 1 × 1 Sr–Se × 2 × 2	2.6465(4) 2.765(3) 2.870(4) 2.930(3) 3.1253(7) 3.1406(7)	2.617(2) 2.787(4) 2.876(4) 2.904(4) 3.109(3) 3.137(2)	2.597(2) 2.785(4) 2.885(3) 2.918(4) 3.113(2) 3.146(2)	2.609(2) 2.784(4) 2.874(5) 2.915(4) 3.117(3) 3.155(3)
Fe1–O × 2 Fe1–Se × 4	2.029(4) 2.7225(4)	2.011(3) 2.738(2)	1.982(3) 2.738(2)	1.992(4) 2.708(2)
Fe2–O × 2 × 1 Fe2–Se × 1 × 1 × 1	2.0059(3) 2.0878(9) 2.7659(10) 2.8740(11) 2.9017(11)	2.0084(4) 2.082(2) 2.714(3) 2.905(3) 2.918(3)	2.0076(3) 2.103(1) 2.721(3) 2.889(3) 2.894(2)	2.0078(4) 2.092(2) 2.754(3) 2.870(3) 2.880(3)
Regime	Paramagnetic	Paramagnetic	Fe2 ordered	Fe1 and Fe2 ordered
Basis expansion of nuclear cell	-	-	[2,0,0], [0,1,0], [0,0,2]	[2,0,0], [0,2,0], [0,0,2]
origin	-	-	(-1/4,0,1/2)	(0,0,0)
Magnetic symmetry (BNS)	-	-	B_ab2_1m(36.178)*	I_ab (9.40)*
K vector	-	-	[½, 0, ½]	[½, 0, ½] , [½,½, 0]
Fe1 |spin| along *a*, *b*, *c* (μ_B)	-	-	-	3.10(2), 1.34(7), 0
Fe1 total spin (μ_B)	-	-	-	3.38(3)
Fe2 |spin| along *a*, *b*, *c* (μ_B)	-	-	0, 0, 3.01(1)	0.69(2), 0.59(5), 3.18(1)
Fe2 total spin (μ_B)	-	-	3.01(1)	3.31(1)

*****non-standard settings of the magnetic space groups have been used to keep the directions of the lattice parameters consistent with the nuclear structure.

Mössbauer Spectroscopy.

The temperature dependence of the Mössbauer spectra has been described and interpreted by Lai *et al.*[15] Here we show the evolution of the spectra in the region from just above T_{N1} to just below T_{INC} spanning the region where the magnetic ordering of the Fe2 moments is incommensurate and the Fe1 moments do not participate in long range order. The data and fits in Figure 13 show the onset of magnetic order between 125 K and 110 K and the evolution to 80 K, below T_{INC}. At 125 K (Figure 13) in the paramagnetic region, the data are modelled by two doublets. The more numerous Fe2 moments produce a doublet with a chemical shift (relative to a thin Fe foil) of $\delta = 1.001(2)$ mm s^{-1} and with a quadrupole splitting of $\Delta E_{\mathrm{Q}} = 1.897(8)$ mm s^{-1}. The remaining doublet is ascribed to the Fe1 moments ($\delta = 0.963(4)$ mm s^{-1}; $\Delta E_{\mathrm{Q}} = 1.46(1)$ mm s^{-1}). As magnetic ordering occurs, the majority signal due to the Fe2 sites is described by a sextet confirming that it is the Fe2 moments that are participating in long range magnetic order below T_{N1} (see the potential ambiguity described above in the analysis of the NPD data). At 80 K (Figure 13), below T_{INC}, the signal due to these Fe2 moments is described by a highly asymmetric sextet arising from the local magnetic field, B_{hf}, due to the magnetic ordering and the quadrupole splitting due to the asymmetric coordination environment.[43] The minority Fe1 signal persists as a quadrupole doublet. In the region between T_{N1} and T_{INC}, where the NPD data show incommensurate magnetic ordering of the Fe2 moments, the Fe2 sextet in the Mössbauer spectrum exhibits very broad lines. The data in this region (110 K and 97 K in Figure 13) were modelled using a quadrupole splitting similar to that used in the paramagnetic region above T_{N1} and in the commensurately ordered region below T_{INC}, and a single value for the local magnetic field that steadily increased with decreasing temperature (Figure 14(a)), but they required much broader line widths in this region (Figure 14(b)) consistent with the spin density wave type order reflecting a wide range of local magnetic fields experienced by the ensemble of Fe2 ions. For discussion of the Mössbauer spectra at lower temperatures where Fe1 undergoes magnetic ordering the reader is referred to the data and analysis of Lai *et al.*[15]

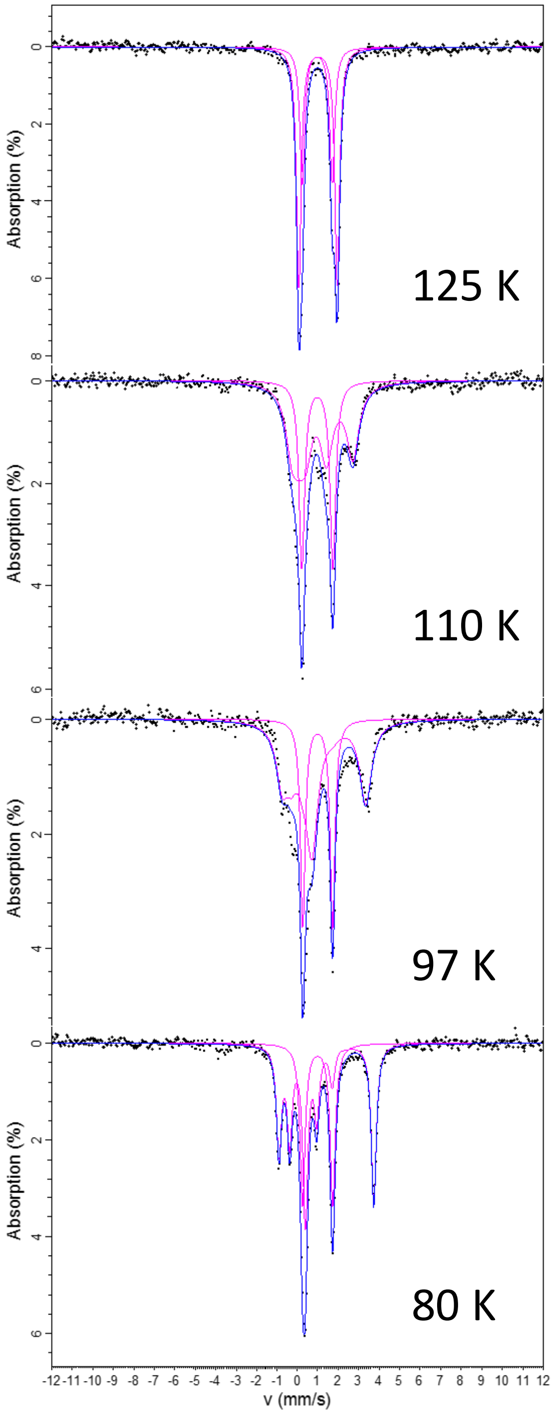

Figure 13. Mössbauer spectra measured through the transitions T_{N1} and T_{INC}. Isomer shift relative to room temperature thin α-Fe foil. Fitting parameters are given in Table 2.

Table 2. Summary of Mössbauer parameters of fit components, relative to room temperature α-Fe.

Temp (K)	Site	δ (mm s^{-1})	ΔE_Q (mm s^{-1})	η	B_{hf} (T)	HWHM (mm s^{-1})	Area (%)	Reduced Chi^2
125	Fe1	0.96	1.46			0.15	37	0.784
	Fe2	1.00	1.88			0.14	63	
110	Fe1	0.97	1.52			0.17	37	1.350
	Fe2	1.06	1.83*	0.7*	4.16	0.36	63	
97	Fe1	0.98	1.45			0.14	34	2.190
	Fe2	1.00	1.83*	0.7*	8.49	0.35	66	
80	Fe1	0.98	1.47			0.15	34	0.840
	Fe2	1.03	1.71	0.7	11.11	0.15	66	
± 1		± 0.02	± 0.02		± 0.5	± 0.01	± 1	

*Quadrupole splitting, ΔE_Q, and asymmetry, η, fixed in the incommensurate region.

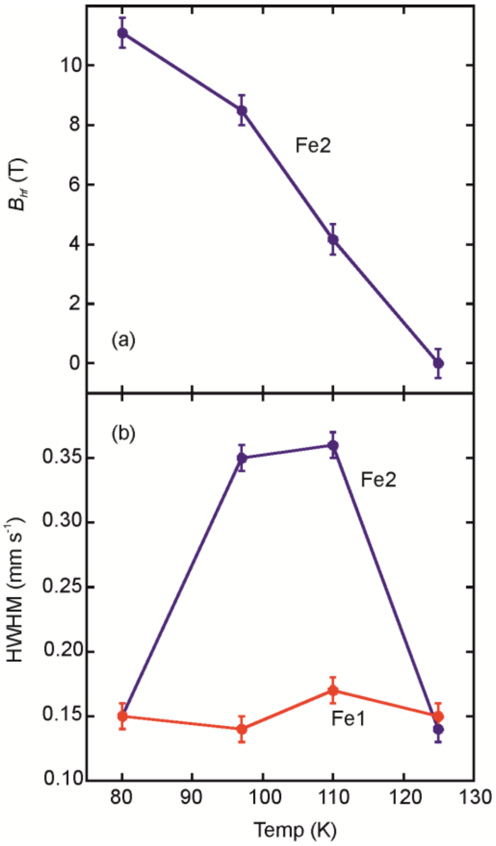

Figure 14. (a) The evolution of the mean hyperfine field, B_{hf}, for the Fe2 sites on cooling through T_{N1} and T_{INC}. (b) The evolution of the linewidths (expressed as half-width at half-maximum (HWHM)) for the Fe1 and Fe2 signals on cooling through T_{N1} and T_{INC}. The broader widths in the region of the incommensurate spin density wave order of the Fe2 moments are ascribed to the range of hyperfine fields experienced by these sites. See Table 2.

Conclusions

$Sr_2Fe_3Se_2O_3$ with two unusual and highly anisotropic environments for Fe^{2+} ions shows a complex succession of magnetic ordering transitions. Neutron powder diffraction measurements unveil the origin of the complexity in the magnetic susceptibility and Mössbauer spectra previously described[15] and reveal an additional region of magnetic behaviour where the onset of long range magnetic ordering on one of the Fe sublattices (Fe2) on cooling results first of all in an incommensurate region of long range order, presumably driven by frustration of some of the weaker exchange interactions. The lowest temperature magnetic structure is dictated by the interactions between the two sublattices of long-range-ordered Fe moments. Given the complexity of the magnetic structures found for compounds composed of these highly anisotropic transition metal coordination environments[26,42] there is scope for tuning the details of the exchange interactions by chemical substitution on the transition metal, chalcogenide and electropositive metal sites.

Associated Content.

Supporting Information

The Supporting Information (.pdf) is available free of charge on the ACS Publications website at DOI:XXXXX.: further Rietveld refinements and diffractograms, tables of refinement results and further discussion of the magnetic models.

Author Information.

SJC (Cassidy) prepared the samples and performed the diffraction and magnetometry measurements. FO, PM and SJC (Cassidy) measured and interpreted the NPD data. JH performed and interpreted the electron diffraction measurements. AS and PAB performed and interpreted the Mössbauer spectroscopy measurements. SJC (Cassidy and Clarke) conceived the project and wrote the paper with input from all co-authors. The authors declare no competing financial interest.

Corresponding Author.

*email: simon.clarke@chem.ox.ac.uk

Acknowledgements.

We acknowledge the financial support of the EPSRC (Grants EP/I017844/1, EP/P018874/1 and EP/M020517/1), and the Leverhulme Trust (RPG-2014-221). We thank the ESTEEM2 network for enabling the electron microscopy investigations, the ISIS facility for the award of beamtime on WISH (RB1610357), and the Diamond Light Source Ltd for the award of beam time on I11 (allocation EE13284). We thank Dr C. Murray, Dr S. Day and Dr A. Baker for assistance on I11 and Dr M Coduri and Dr A N Fitch for assistance on ID22.

References

(1) Hiramatsu, H.; Kamihara, Y.; Yanagi, H.; Ueda, K.; Kamiya, T.; Hirano, M.; Hosono, H. Layered mixed-anion compounds: Epitaxial growth, active function exploration, and device application. *J. Eur. Ceram. Soc.* **2009**, *29*, 245–253.

(2) Ueda, K.; Inoue, S.; Hirose, S.; Kawazoe, H.; Hosono, H. Transparent p -type semiconductor: LaCuOS layered oxysulfide. *Appl. Phys. Lett.* **2000**, *77*, 2701–2703.

(3) Scanlon, D. O.; Watson, G. W. $(Cu_2S_2)(Sr_3Sc_2O_5)$-A layered, direct band gap, p-type transparent conducting oxychalcogenide: A theoretical analysis. *Chem. Mater.* **2009**, *21*, 5435–5442.

(4) Zhao, L. D.; Berardan, D.; Pei, Y. L.; Byl, C.; Pinsard-Gaudart, L.; Dragoe, N. $Bi_{1-x}Sr_xCuSeO$ oxyselenides as promising thermoelectric materials. *Appl. Phys. Lett.* **2010**, *97*, 092118.

(5) Kamihara ,Y.; Watanabe, T.; Hirano, M.; Hosono H. Iron-Based Layered Superconductor $La[O_{1-x}F_x]FeAs$ (x = 0.05–0.12) with T_c = 26 K. **2008**, *130*, 3296–3297.

(6) Hsu, F.-C.; Luo, J.-Y.; Yeh, K.-W.; Chen, T.-K.; Huang, T.-W.; Wu, P. M.; Lee, Y.-C.; Huang, Y.-L.; Chu, Y.-Y.; Yan, D.-C.; Wu, M.-K. Superconductivity in the PbO-type structure -FeSe. *Proc. Natl. Acad. Sci.* **2008**, *105*, 14262–14264.

(7) Sun, H.; Woodruff, D. N.; Cassidy, S. J.; Allcroft, G. M.; Sedlmaier, S. J.; Thompson, A. L.; Bingham, P. A.; Forder, S. D.; Cartenet, S.; Mary, N.; Ramos, S.; Foronda, F. R.; Williams, B. H.; Li, X.; Blundell, S. J.; Clarke, S. J. Soft chemical control of superconductivity in lithium iron selenide hydroxides $Li_{1-x}Fe_x(OH)Fe_{1-y}Se$. *Inorg. Chem.* **2015**, *54*, 1958–1964.

(8) Clarke, S. J.; Adamson, P.; Herkelrath, S. J. C.; Rutt, O. J.; Parker, D. R.; Pitcher, M. J.; Smura, C. F. Structures, Physical Properties, and Chemistry of Layered Oxychalcogenides and Oxypnictides. *Inorg. Chem.* **2008**, *47*, 8473–8486.

(9) Mayer, J. M.; Schneemeyer, L. F.; Siegrist, T.; Waszczak, J. V.; Van Dover, B. New Layered Iron-Lanthanum-Oxide-Sulfide and -Selenide Phases: $Fe_2La_2O_3E_2$(E = S, Se). *Angew. Chemie Int. Ed. English* **1992**, *31*, 1645–1647.

(10) Huh, S.; Prots, Y.; Adler, P.; Hao Tjeng, L.; Valldor, M. Synthesis and Characterization of Frustrated Spin Ladders $SrFe_2S_2O$ and $SrFe_2Se_2O$. *Eur. J. Inorg. Chem.* **2015**, *2015*, 2982–2988.

(11) Cassidy, S. J.; Batuk, M.; Batuk, D.; Hadermann, J.; Woodruff, D. N.; Thompson, A. L.; Clarke, S. J. Complex Microstructure and Magnetism in Polymorphic CaFeSeO. *Inorg. Chem.* **2016**, *55*, 10714–10726.

(12) Han, F.; Wang, D.; Malliakas, C. D.; Sturza, M.; Chung, D. Y.; Wan, X.; Kanatzidis, M. G. (CaO)(FeSe): A Layered Wide-Gap Oxychalcogenide Semiconductor. *Chem. Mater.* **2015**, *27*, 5695–5701.

(13) Lai, K. T.; Komarek, A. C.; Fernández-Díaz, M. T.; Chang, P. S.; Huh, S.; Rosner, H.; Kuo, C. Y.; Hu, Z.; Pi, T. W.; Adler, P.; Ksenofontov, V.; Tjeng, L. H.; Valldor, M. Canted Antiferromagnetism on Rectangular Layers of Fe^{2+} in Polymorphic CaFeSeO. *Inorg. Chem.* **2017**, *56*, 4271–4279.

(14) Delacotte, C.; Pérez, O.; Pautrat, A.; Berthebaud, D.; Hébert, S.; Suard, E.; Pelloquin, D.; Maignan, A. Magnetodielectric Effect in Crystals of the Noncentrosymmetric CaOFeS at Low Temperature. *Inorg. Chem.* **2015**, *54*, 6560–6565.

(15) Lai, K. T.; Adler, P.; Prots, Y.; Hu, Z.; Kuo, C.-Y.; Pi, T.-W.; Valldor, M. Successive Phase Transitions in Fe^{2+} Ladder Compounds $Sr_2Fe_3Ch_2O_3$ (Ch = S, Se). *Inorg. Chem.* **2017**, *56*, 12606–12614.

(16) Lai, K. T.; Valldor, M. Coexistence of spin ordering on ladders and spin dimer formation in a new-structure-type compound $Sr_2Co_3S_2O_3$. *Sci. Rep.* **2017**, *7*, 43767.

(17) Thompson, S. P.; Parker, J. E.; Potter, J.; Hill, T. P.; Birt, A.; Cobb, T. M.; Yuan, F.; Tang, C. C. Beamline I11 at Diamond: A new instrument for high resolution powder diffraction. *Rev. Sci. Instrum.* **2009**, *80*, 075107.

(18) Chapon, L. C.; Manuel, P.; Radaelli, P. G.; Benson, C.; Perrott, L.; Ansell, S.; Rhodes, N. J.; Raspino, D.; Duxbury, D.; Spill, E.; Norris, J. WISH: The New Powder and Single Crystal Magnetic Diffractometer on the Second Target Station. *Neutron News* **2011**, *22*, 22–25.

(19) Coelho, A. A. TOPAS Academic Version 5, Coelho Software, Brisbane, Australia. **2012**.

(20) Kovats, T. A.; Walker, J. C. Mössbauer absorption in Fe^{57} in metallic iron from the Curie point to the γ-δ Transition. *Phys. Rev.* **1969**, *181*, 610–618.

(21) Rancourt, D. *Recoil Mössbauer Spectral Analysis Software*. **1998**. www.academia.edu/1072429/

(22) Kabbour, H.; Janod, E.; Corraze, B.; Danot, M.; Lee, C.; Whangbo, M.-H.; Cario, L. Structure and Magnetic Properties of Oxychalcogenides $A_2F_2Fe_2OQ_2$ (A = Sr, Ba; Q = S, Se) with Fe_2O Square Planar Layers Representing an Antiferromagnetic Checkerboard Spin Lattice. *J. Am. Chem. Soc.* **2008**, *130*, 8261–8270.

(23) He, J. B.; Wang, D. M.; Shi, H. L.; Yang, H. X.; Li, J. Q.; Chen, G. F. Synthesis, structure, and magnetic properties of the layered iron oxychalcogenide $Na_2Fe_2Se_2O$. *Phys. Rev. B* **2011**, *84*, 205212.

(24) Takeiri, F.; Matsumoto, Y.; Yamamoto, T.; Hayashi, N.; Li, Z.; Tohyama, T.; Tassel, C.; Ritter, C.; Narumi, Y.; Hagiwara, M.; Kageyama, H. High-pressure synthesis of the layered iron oxyselenide $BaFe_2Se_2O$ with strong magnetic anisotropy. *Phys. Rev. B* **2016**, *94*, 184426.

(25) Wang, C.; Tan, M. Q.; Feng, C. M.; Ma, Z. F.; Jiang, S.; Xu, Z. A.; Cao, G. H.; Matsubayashi, K.; Uwatoko, Y. $La_2Co_2Se_2O_3$: A quasi-two-dimensional mott insulator with unusual cobalt spin state and possible orbital ordering. *J. Am. Chem. Soc.* **2010**, *132*, 7069–7073.

(26) Free, D. G.; Withers, N. D.; Hickey, P. J.; Evans, J. S. O. Synthesis, Structure and Properties of Several New Oxychalcogenide Materials with the General Formula $A_2O_2M_2OSe_2$ (A = La−Sm, M = Fe, Mn). *Chem. Mater.* **2011**, *23*, 1625–1635.

(27) Ni, N.; Climent-Pascual, E.; Jia, S.; Huang, Q.; Cava, R. J. Physical properties and magnetic structure of the layered oxyselenide $La_2O_3Mn_2Se_2$. *Phys. Rev. B* **2010**, *82*, 214419.

(28) Valldor, M.; Merz, P.; Prots, Y.; Schnelle, W. Bad-Metal-Layered Sulfide Oxide CsV_2S_2O. *Eur. J. Inorg. Chem.* **2016**, *2016*, 23–27.

(29) Zhang, H.; Wu, X.; Li, D.; Jin, S.; Chen, X.; Zhang, T.; Lin, Z.; Shen, S.; Yuan, D.; Chen, X. $Ca_2O_3Fe_{2.6}S_2$: an antiferromagnetic Mott insulator at proximity to bad metal. *J. Phys. Condens. Matter* **2016**, *28*, 145701.

(30) Nitsche, F.; Niklaus, R.; Johrendt, D. New Polymorphs of $RE_2FeSe_2O_2$ (RE = La, Ce). *Zeitschrift für Anorg. und Allg. Chemie* **2014**, *640*, 2897–2902.

(31) Dugué, J.; Tien, V.; Laruelle, P. Structure de l’oxysulfure de lanthane et de vanadium, $La_5V_3O_7S_6$. *Acta Crystallogr. Sect. C Cryst. Struct. Commun.* **1985**, *41*, 1146–1148. DOI:

(32) Cody, J. A.; Ibers, J. A. Synthesis and Characterization of the New Rare-Earth/Transition-Metal Oxysulfides $La_6Ti_2S_8O_5$ and $La_4Ti_3S_4O_8$. *J. Solid State Chem.* **1995**, *114*, 406–412.

(33) Campbell, B. J.; Stokes, H. T.; Tanner, D. E.; Hatch, D. M. ISODISPLACE : a web-based tool for exploring structural distortions. *J. Appl. Crystallogr.* **2006**, *39*, 607–614.

(34) Rodríguez-Carvajal, J. Recent advances in magnetic structure determination by neutron powder diffraction. *Phys. B Phys. Condens. Matter* **1993**, *192*, 55–69.

(35) Miller, S. C.; Love, W. F. *Tables of irreducible representations of space groups and co-representations of magnetic space groups*; Pruett Press: Boulder Colo., **1967**.

(36) Cracknell, A. P.; Davies, B. L.; Miller, S. C.; Love, W. F. *Kronecker product tables, Vol. 1, General introduction and tables of irreducible representations of space groups.*; IFI/Plenum: New York, **1979**.

(37) *Magnetic Group Tables*; Litvin, D. B., Ed.; International Union of Crystallography: Chester, England, **2013**.

(38) Yamaguchi, H.; Miyagai, H.; Yoshida, M.; Takigawa, M.; Iwase, K.; Ono, T.; Kase, N.; Araki, K.; Kittaka, S.; Sakakibara, T.; Shimokawa, T.; Okubo, T.; Okunishi, K.; Matsuo, A.; Hosokoshi, Y. Field-induced incommensurate phase in the strong-rung spin ladder with ferromagnetic legs. *Phys. Rev. B* **2014**, *89*, 220402.

(39) Hsieh, D.; Qian, D.; Berger, R. F.; Cava, R. J.; Lynn, J. W.; Huang, Q.; Hasan, M. Z. Unconventional spin order in the triangular lattice system $NaCrO_2$: A neutron scattering study. *Phys. B Condens. Matter* **2008**, *403*, 1341–1343.

(40) Fang, C.; Hu, J. An effective model of magnetoelectricity in multiferroics RMn_2O_5. *Europhys. Lett.* **2008**, *82*, 57005.

(41) Keller, L.; Doennl, A.; Kitazawa, H.; van den Brandt, B. Geometrical frustration and incommensurate magnetic ordering in CePdAl: a low-temperature neutron-diffraction study. *Appl. Phys. A Mater. Sci. Process.* **2002**, *74*, s686–s688.

(42) Zhao, L. L.; Wu, S.; Wang, J. K.; Hodges, J. P.; Broholm, C.; Morosan, E. Quasi-two-dimensional noncollinear magnetism in the Mott insulator $Sr_2F_2Fe_2OS_2$. *Phys. Rev. B* **2013**, *87,* 020406.

(43) Dyar, M. D.; Agresti, D. G.; Schaefer, M. W.; Grant, C. A.; Sklute, E. C. Mössbauer Spectroscopy of Earth and Planetary Materials. *Annu. Rev. Earth Planet. Sci.* **2006**, *34*, 83–125.

For Table of Contents Only

$Sr_2Fe_2Se_2O_3$ displays complex magnetic ordering over two Fe^{2+} sublattices which is probed using powder neutron diffraction.

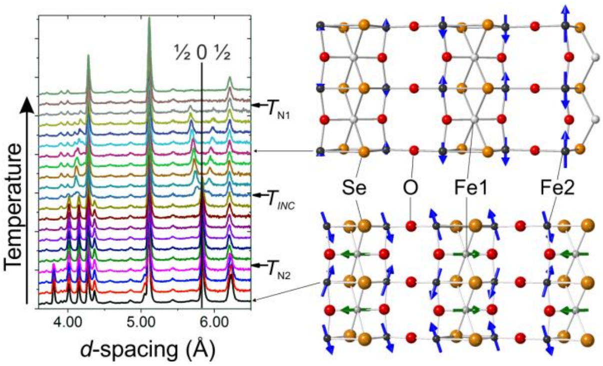

Complex magnetic ordering in the oxide selenide $Sr_2Fe_3Se_2O_3$

Simon J Cassidy,[1] Fabio Orlandi,[2] Pascal Manuel,[2] Joke Hadermann,[3] Alex Scrimshire,[4] Paul A Bingham[4] and Simon J Clarke[1*]

[1]Department of Chemistry, University of Oxford, Inorganic Chemistry Laboratory, South Parks Road, Oxford, OX1 3QR, UK. [2]ISIS Facility, STFC Rutherford Appleton Laboratory, Harwell Oxford, Didcot OX11 0QX, United Kingdom. [3] Electron Microscopy for Materials Science (EMAT), University of Antwerp, Groenenborgerlaan 171, B-2020 Antwerp, Belgium., [4] Materials and Engineering Research Institute, Faculty of Arts, Computing, Engineering and Sciences, Sheffield Hallam University, City Campus, Howard Street, Sheffield, S1 1WB,UK.

Supplementary Material

*Corresponding author

email: simon.clarke@chem.ox.ac.uk

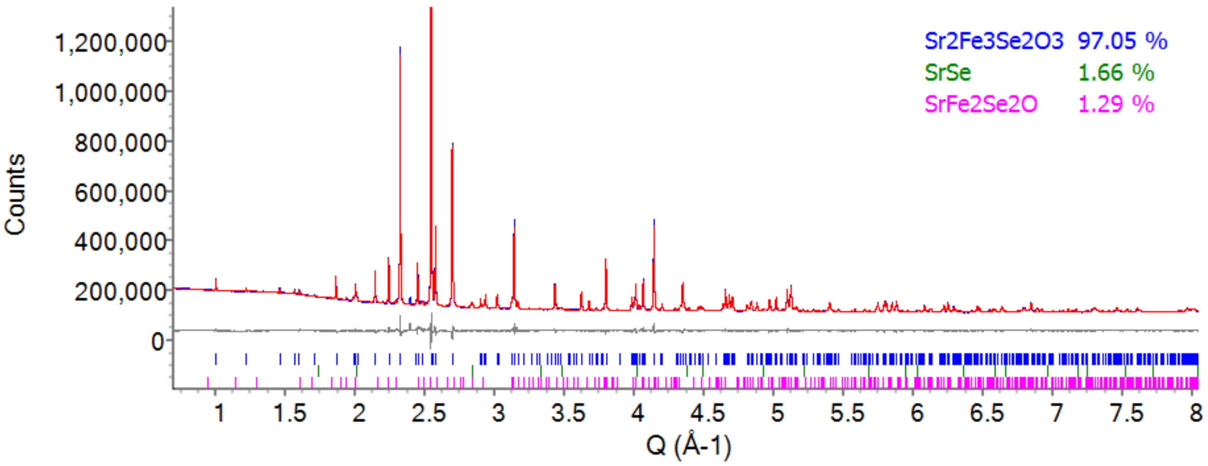

Figure S1 Rietveld refinement against PXRD pattern of $Sr_2Fe_3Se_2O_3$ sample ***A*** taken at room temperature using the Mythen detector of the I11 diffractometer at Diamond Light Source.

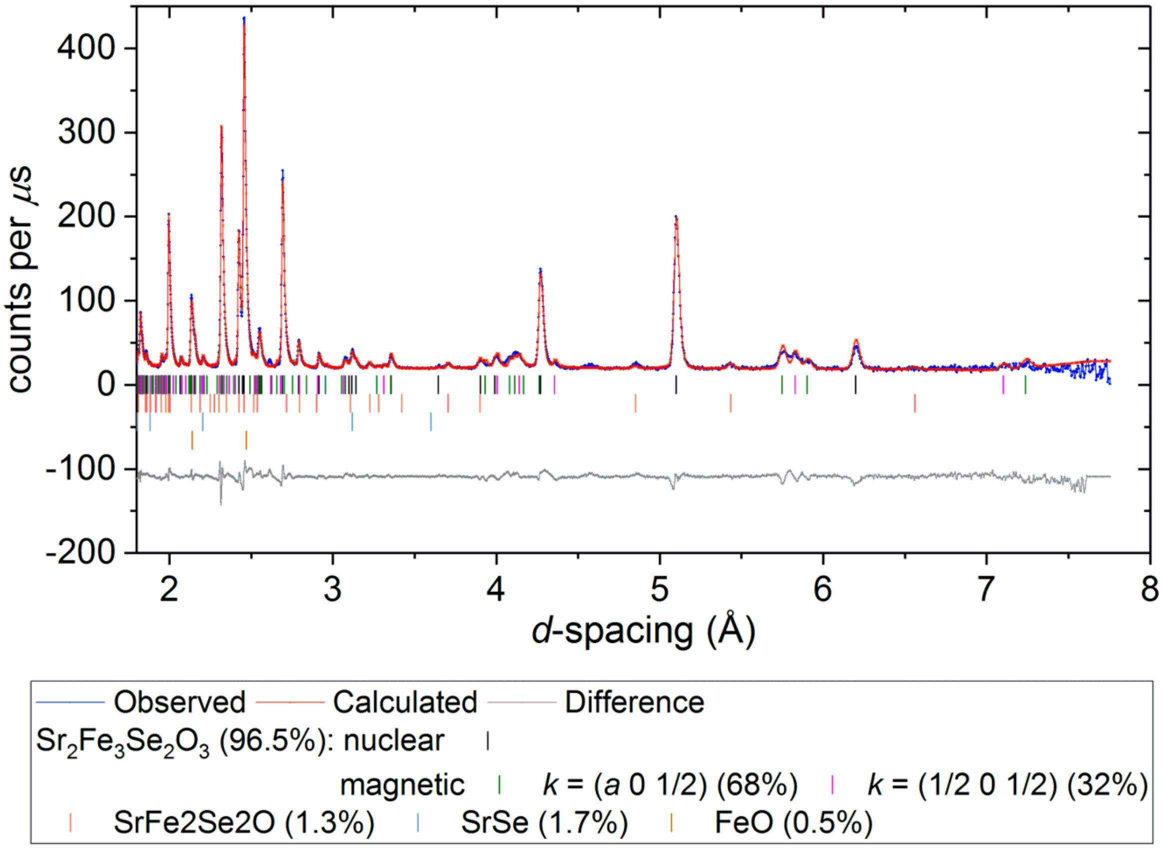

Figure S2 Rietveld refinement of $Sr_2Fe_3Se_2O_3$ sample A at 92 K showing the coexistence of the commensurate and incommensurate magnetic phases at T_{INC}. The material shows only the commensurate magnetic structure at and below 91 K, and only the incommensurate magnetic structure at 93 K up to T_{N1}.

Description of the magnetic models using ISODISTORT

As described in the main text, between 55 (T_{N2}) and 91 K (T_{INC}), one of the two Fe sites shows commensurate magnetic order with k-point U (½, 0, ½). The neutron diffraction data may be described with either the Fe2 sites; using mU2(a,0) modes with mU2[Fe2:h:mag]A’_1(a) constrained to be equal to minus mU2[Fe2:h:mag]A’_2(a), or the Fe1 sites; using the mU1(a,0) mode [Fe1:a:mag]mU1Ag(a). Equivalent fits can be achieved with either site, however using the Fe1 sites gives an ordered moment at 55K of 4.75 μ_B which is unrealistic for an Fe^{2+} ion. The conclusion that it is the Fe2 sites ordering in this regime is consistent with the Mössbauer data, which show the more abundant site to be the one that is ordered. An equivalent case occurs in the incommensurate region between T_{INC} and 118K (T_{N1}), in which the magnetic scattering occurs with k-point A (a, 0, ½) and can be described by either the Fe2 site with mA2 modes or Fe1 site with mA1 modes.

Below T_{N2} the Fe1 sites order, with *k* point S (*k*=½, ½, 0). In determining the model, the six ordering modes associated with this k-point for the Fe1 sites were tried: mS3+S4+ [Fe1:a:mag]Bg_1(a), mS3+S4+ [Fe1:a:mag]Bg_1(b), mS3+S4+ [Fe1:a:mag]Bg_2(a), mS3+S4+ [Fe1:a:mag]Bg_2(b), mS1+S2+ [Fe1:a:mag]Ag(a) and mS1+S2+ [Fe1:a:mag]Ag(b). Of these six, a combination of the four mS3+4+ modes: Bg_1(a,a) and Bg_2(a,a) gives a reasonable model, but does not give a satisfactory fit to the data, shown in Figure S3(a). The fit can be improved slightly by allowing all six terms to refine freely {mS3+S4+ Bg_1(a,b), mS3+S4+ Bg_2(a,b), mS1+S2+ Ag(a,b)} but even this gives a poor statistical and visual fit, which indicates that the data cannot be fitted with these modes alone, as shown in Figure S3(b). Inclusion of the Fe2 sites in the model was carried out by refining the combinations of the twelve modes associated with the S k-point for the Fe2 sites alongside those of the Fe1 sites. Of these twelve, only a combination of the mS3+S4+[Fe2:h:mag] modes gave significant improvement to the fit: refining mS3+S4+[Fe2:h:mag]A’’_1(a,a) and mS3+S4+[Fe2:h:mag]A’’_2(a,a) as well as mS3+S4+ [Fe1:a:mag]Bg_1(a,a) and mS3+S4+ [Fe1:a:mag]Bg_2(a,a). This produces a good statistical and visual fit, shown in Figure S3(c), with a reasonable magnetic model. If all 18 terms are allowed to refine freely of one another and produce a nonsensical model, only a minimal improvement in the agreement factor can be achieved (5.4 % vs 5.2 %), indicating the model represents a global minimum in the refinement.

The overall magnetic model uses five parameters to describe the ordering of the 32 Fe2 and 16 Fe1 atoms in the $2a_{\mathrm{nucl}} \times 2b_{\mathrm{nucl}} \times 2c_{\mathrm{nucl}}$ magnetic cell: one for the major component of the Fe2 ordering (described by mU2[Fe2:h:mag]A’_1(a,0) = –mU2[Fe2:h:mag]A’_2(a,0)), two for the Fe1 ordering (described by mS3+4+[Fe1:a:mag]Bg_1(a,a) and mS3+4+[Fe1:a:mag]Bg_2(a,a)), and two for the Fe2 canting (described by –mS3+4+[Fe2:h:mag]A’’_1(a,a) and –mS3+4+[Fe2:h:mag]A’’_2(a,a)). Importantly, the mS3+S4+[Fe2] modes refine to have opposite sign to the mS3+S4+[Fe1] modes, which results in the Fe2 ions being antiferromagnetically aligned with respect to the nearest neighbour Fe1 ions.

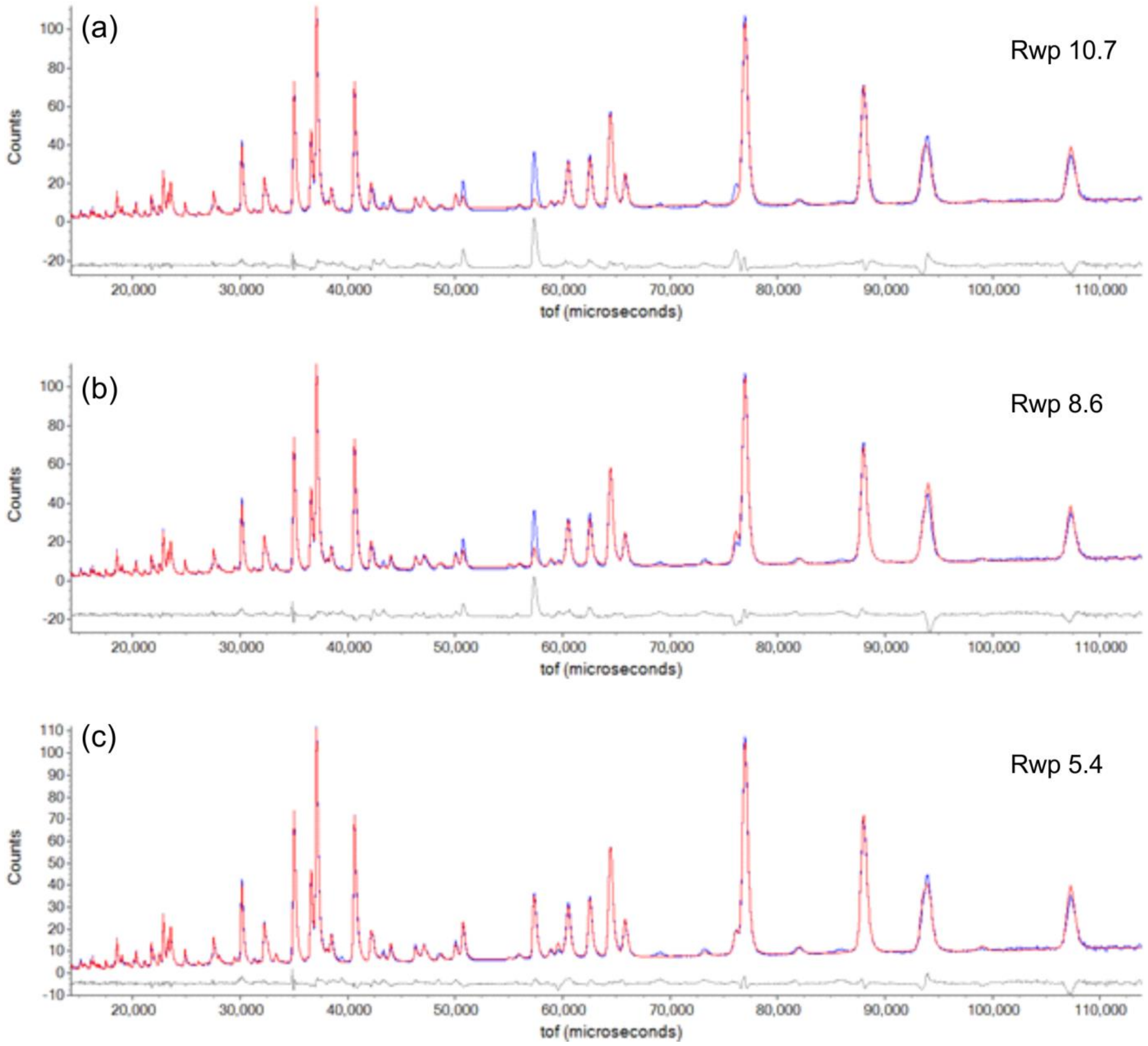

Figure S3 WISH bank 3/8 of a Rietveld refinement of the neutron diffraction pattern of sample ***A*** at 1.5K. **(a)** refinement of the model using only the Fe1 sites to account for the S-point magnetic scattering with all Fe1 atoms carrying the same moment. **(b)** Refinement of the model using only the Fe1 sites to account for the S-point magnetic scattering but allowing the free refinement of the parameters such that different atoms can have different moments. **(c)** Refinement of the model using both the Fe1 and Fe2 sites to account for the S-point magnetic scattering, using a sensible model.

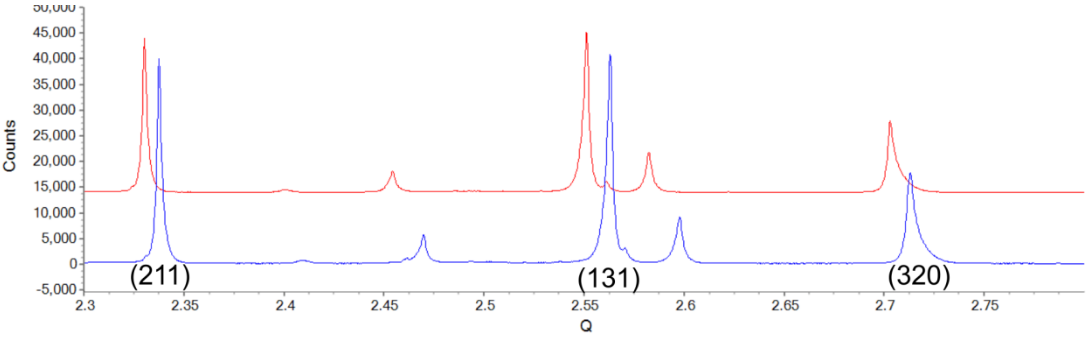

Figure S4 X-ray diffraction patterns of Sample A taken using the MAC detector of the ID22 diffractometer at the ESRF. The red pattern was taken at room temperature and the blue pattern at 5 K. No evidence of splitting in the strongest structural peaks is observed.

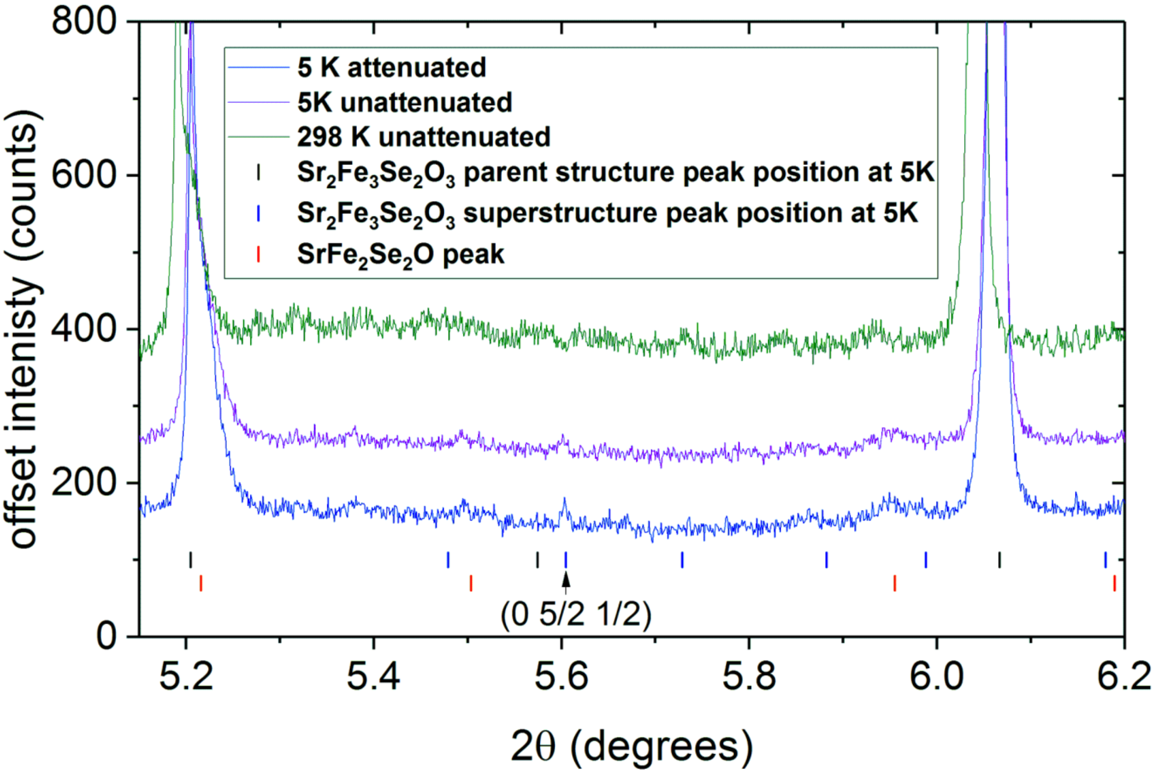

Figure S5 Powder X-ray diffraction of sample ***A*** taken at ID22 (λ=0.35440(Å)). The data taken at 5K (blue line) show the presence of a very weak peak at 5.6° coincident with the position of the 0 5/2 ½ reflection expected from the magnetic structure and symmetry analysis. This peak appears weaker in the pattern taken with the unattenuated beam (purple line), which while measured in the cryostat at 5K is estimated to be between 30 and 60 K based on the lattice parameters due to beam heating. The peak is absent in the room temperature diffraction pattern (green line).Note that the maximum peak height observed in the pattern was 40,000 counts.

Tables of unit cell information in the paramagnetic regime.

Table S1 Refined atomic parameters against synchrotron powder diffraction data for sample ***B***, corresponding to the data in Table 1 in the main paper. Peakshape asymmetry was observed in this high resolution data. Attempting to refine the asymmetry as 2 phases with different lattice parameters produced an improved fit, but no differences in the occupancies or positions of the atoms could be discerned between the phases. Since no physical origin for this asymmetry could be established, it was instead handled with an arbitrary asymmetric peakshape function.

Instrument	I11
Temperature	Room temperature
Nuclear symmetry	*Pbam* (55)
a **(Å)**	7.8121(2)
b **(Å)**	10.23747(9)
c **(Å)**	3.99388(5)
V (Å^3)	319.413(7)
Density (g cm^{-3})	5.70486(9)
R_{wp} **(%)**	5.22
χ^2	1.56
R_{Bragg}	2.03

Atom	**Site**	***x***	***y***	***z***	U_{11} **(Å^2)**	U_{22} **(Å^2)**	U_{33} **(Å^2)**	U_{12} **(Å^2)**
Sr1	4*g*	0.09160(7)	0.34920(6)	0	0.0158(5)	0.0156(4)	0.0136(4)	–0.0007(4)
Fe1	2*a*	0	0	0	0.0136(8)	0.0191(7)	0.0141(8)	0.0002(6)
Fe2	4*h*	0.2588(1)	0.08825(8)	0.5	0.0129(6)	0.0188(4)	0.0120(5)	0.0010(4)
Se1	4*h*	0.40095(8)	0.33574(6)	0.5	0.0128(5)	0.0122(4)	0.0122(4)	0.0005(4)
O1	2*d*	0	0.5	0.5	0.004(2)	0.004(2)	0.004(2)	0*
O2	4*g*	0.2346(5)	0.0846(3)	0	0.017(1)	0.017(1)	0.017(1)	0*

* not refined: displacement ellipsoids for the oxide sites were refined as isotropic.

Table S2 refinement parameters from WISH at 135K for sample ***B***, corresponding to the data in Table 1 in the main paper.

Instrument	WISH
Temperature	135 K
Nuclear symmetry	*Pbam* (55)
***a* (Å)**	7.8003(2)
***b* (Å)**	10.2112(3)
***c* (Å)**	3.99121(9)
V (Å^3)	317.97(1)
Density (g cm^{-3})	5.7308(2)
R_{wp} (%)	4.10
χ^2	1.06
R_{Bragg}	1.37

Atom	**Site**	***x***	***y***	***z***	**U_{11} (Å^2)**	**U_{22} (Å^2)**	**U_{33} (Å^2)**	**U_{12} (Å^2)**
Sr1	4*g*	0.0908(3)	0.3494(2)	0	0.019(2)	0.017(3)	0.015(2)	0.004(2)
Fe1	2*a*	0	0	0	0.049(3)	0.023(3)	0.045(4)	0.024(2)
Fe2	4*h*	0.2604(2)	0.0897(2)	0.5	0.013(2)	0.025(2)	0.015(1)	–0.001(1)
Se1	4*h*	0.4003(3)	0.3330(2)	0.5	0.020(2)	0.014(2)	0.035(2)	0.001(2)
O1	2*d*	0	0.5	0.5	0.006(4)	0.008(4)	0.017(4)	–0.007(3)
O2	4*g*	0.2318(4)	0.0863(3)	0	0.050(4)	0.015(3)	0.035(2)	0.003(3)

Tables of structural information in the Fe2 ordered regime

Table S3 refinement parameters from WISH at 55K for the nuclear cell of sample ***B***, corresponding to the data in Table 1 in the main paper.

Instrument	WISH
Temperature	55 K
Nuclear symmetry	*Pbam* (55)
***a* (Å)**	7.7963(2)
***b* (Å)**	10.2008(3)
***c* (Å)**	3.98951(9)
V (Å^3)	317.18(1)
Density (g cm^{-3})	5.7452(2)
R_{wp} (%)	4.55
χ^2	1.17
R_{Bragg}	1.55

Atom	Site	*x*	*y*	*z*	U_{11} (Å^2)	U_{22} (Å^2)	U_{33} (Å^2)	U_{12} (Å^2)
Sr1	4*g*	0.0889(3)	0.3519(2)	0	0.019(2)	0.018(3)	0.019(2)	–0.001(2)
Fe1	2*a*	0	0	0	0.057(4)	0.015(3)	0.056(4)	0.023(2)
Fe2	4*h*	0.2569(2)	0.0893(2)	0.5	0.020(2)	0.027(2)	0.012(1)	0.003(2)
Se1	4*h*	0.4000(3)	0.3327(2)	0.5	0.021(2)	0.030(3)	0.030(2)	–0.008(2)
O1	2*d*	0	0.5	0.5	0.001(4)	0.002(4)	0.008(4)	0.001(3)
O2	4*g*	0.2278(3)	0.0862(3)	0	0.038(4)	0.009(3)	0.051(3)	–0.001(3)

Table S4 refinement parameters from WISH at 55K for the magnetic cell of sample ***B***, corresponding to the data in Table 1 in the main paper.

Instrument	WISH
Temperature	55 K
magnetic symmetry	B_ab2_1m (36.178)*
***a* (Å)**	15.5911(4)‡
***b* (Å)**	10.1997(3)‡
***c* (Å)**	7.9782(2)‡
***V* (Å^3)**	1268.72(5)‡
Density (g cm^{-3})	5.7452(2)
R_{wp} (%)	4.55
χ^2	1.17
R_{Bragg}	2.30

Atom	***site***	***x***	***y***	***z***		**μ_x (μ_B)**	**μ_y (μ_B)**	**μ_z (μ_B)**
Fe2_1	8*a*	0.2569(2)	0.0893(2)	0		0	0	3.10(1)
Fe2_2	8*a*	0.5069(2)	0.4107(2)	0		0	0	3.10(1)

*This is a non standard setting of C_amc2_1, used in order maintain the same axis orientation as used for the nuclear cell. The unit cell is a 2*a* × *b* × 2*c* expansion of the nuclear unit cell.

Tables of structural information in the Fe1 and Fe2 ordered regime

Table S5 refinement parameters from WISH at 20K for the nuclear cell of sample ***B***, corresponding to the data in Table 1 in the main paper.

Instrument	WISH
Temperature	20 K
Nuclear symmetry	*Pbam* (55)
***a* (Å)**	7.7945(2)
***b* (Å)**	10.1979(3)
***c* (Å)**	3.9893(1)
***V* (Å^3)**	317.10(1)
Density (g cm^{-3})	5.7465(3)
R_{wp} (%)	4.61
χ^2	1.21
R_{Bragg}	1.99

Atom	**Site**	***x***	***y***	***z***	**U_{11} (Å^2)**	**U_{22} (Å^2)**	**U_{33} (Å^2)**	**U_{12} (Å^2)**
Sr1	4*g*	0.0898(3)	0.3487(3)	0	0.012(2)	0.022(3)	0.017(2)	0.001(2)
Fe1	2*a*	0	0	0	0.039(3)	0.018(3)	0.060(4)	0.015(2)
Fe2	4*h*	0.2599(2)	0.0900(2)	0.5	0.015(2)	0.025(2)	0.007(1)	0.003(2)
Se1	4*h*	0.4003(3)	0.3350(3)	0.5	0.022(2)	0.014(3)	0.024(2)	0.002(2)
O1	2*d*	0	0.5	0.5	0.017(5)	0.006(5)	0.006(4)	–0.007(3)
O2	4*g*	0.2317(4)	0.0860(3)	0	0.052(4)	0.010(3)	0.055(3)	0.008(4)

Table S6 refinement parameters from WISH at 20K for the magnetic cell of sample B, corresponding to the data in Table 1 in the main paper.

Instrument	WISH
Temperature	20 K
magnetic symmetry	$I_a b$* (9.40)
***a* (Å)**	15.5890(4)
***b* (Å)**	20.3958(6)
***c* (Å)**	7.9786(2)
γ(°)	90
V (Å^3)	2536.80(8)
R_{wp} (%)	4.61
χ^2	1.21
R_{Bragg}	2.27

Atom	***site***	***x***	***y***	***z***	**μ_x (μ_B)**	**μ_y (μ_B)**	**μ_z (μ_B)**
Fe1_1	4*a*	0	0	0	3.10(2)	-1.34(7)	0
Fe1_2	4*a*	0.5	0.5	0	3.10(2)	-1.34(7)	0
Fe1_3	4*a*	0.25	0.75	0	-3.10(2)	-1.34(7)	0
Fe1_4	4*a*	0.75	0.25	0	-3.10(2)	-1.34(7)	0
Fe2_1	*8a*	0.12995(11)	-0.04500(10)	0.75	-0.69(2)	0.59(5)	3.18(1)
Fe2_5	*8a*	0.37995(11)	0.79500(10)	0.25	0.69(2)	0.59(5)	-3.18(1)
Fe2_9	*8a*	0.12005(11)	0.70500(10)	0.25	0.69(2)	0.59(5)	-3.18(1)
Fe2_13	*8a*	0.87005(11)	0.04500(10)	0.75	-0.69(2)	0.59(5)	3.18(1)

*This is a non standard setting of space group $C_c c$ (9.40 in BNS notation), used in order maintain the same axis orientation as used for the nuclear cell. The unit cell is a 2*a* × 2*b* × 2*c* expansion of the nuclear unit cell.

.

Figure S6. Rietveld refinements against Neutron Powder Diffraction data of Sample A. patterns at 1.5-91 and 125-150K were refined against with Topas Academic, patterns 92-119K were refined against with FullProf. The 150K refinement in Fullprof is also shown for comparison.

sample A 1.5 K / 90 degree bank

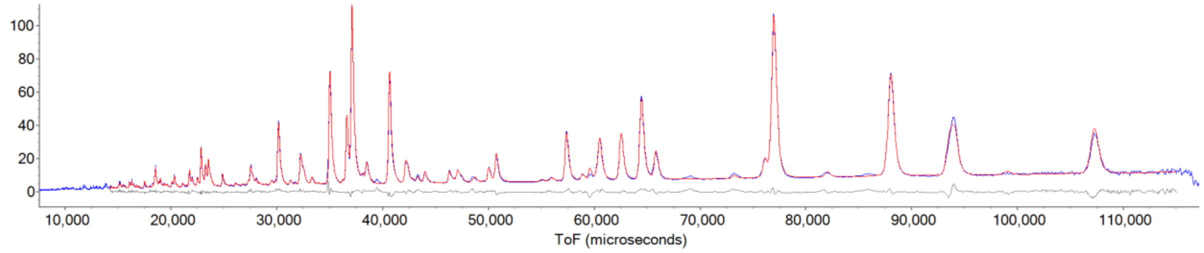

sample A 20 K / 90 degree bank

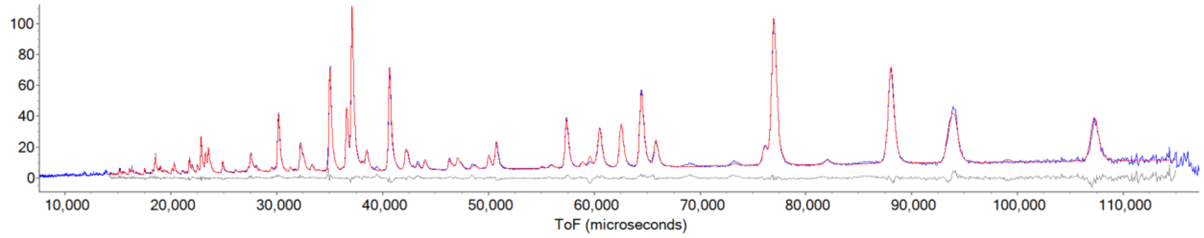

sample A 30 K / 90 degree bank

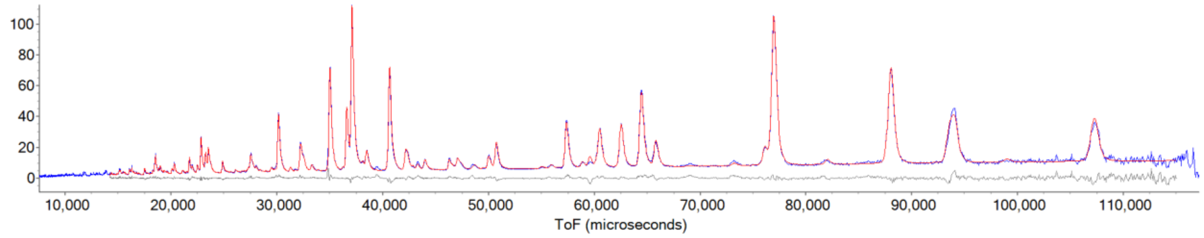

sample A 36 K / 90 degree bank

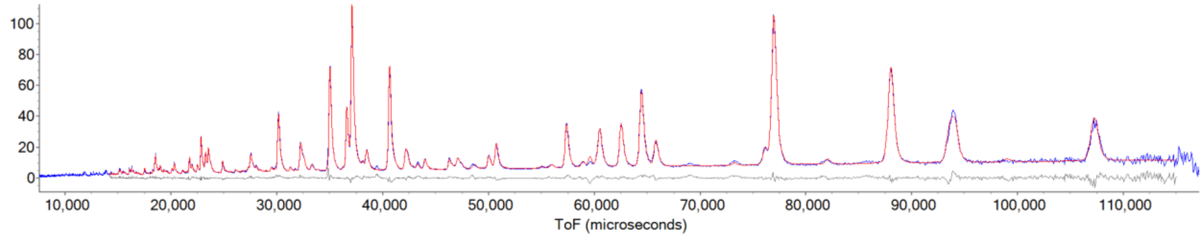

sample A 45 K / 90 degree bank

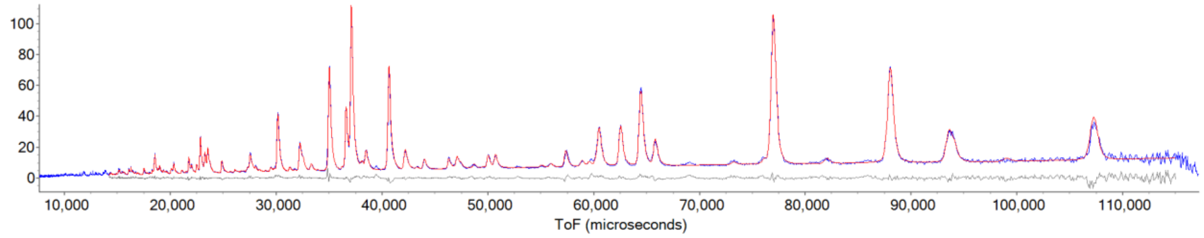

sample A 48 K / 90 degree bank

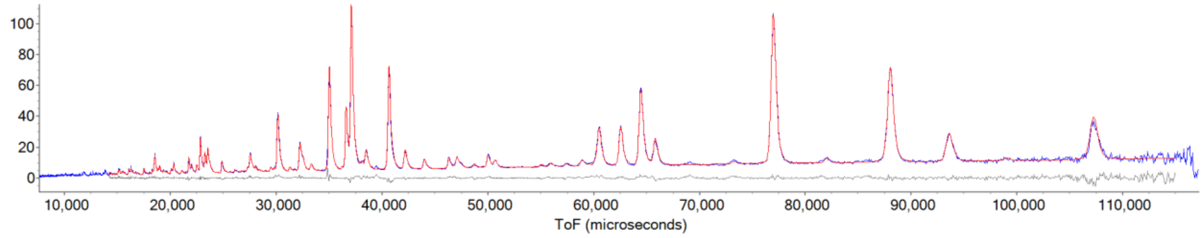

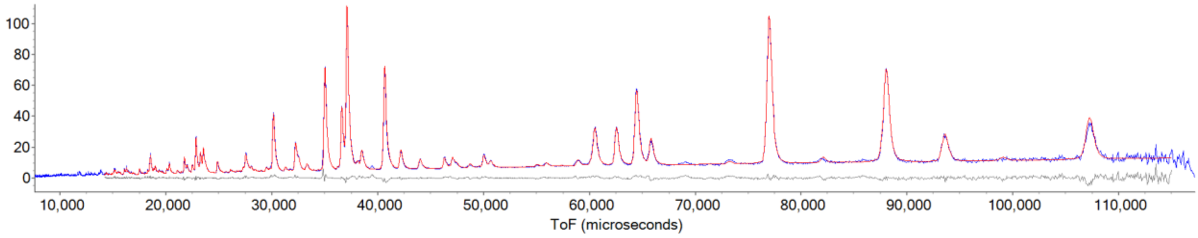
sample A 51 K / 90 degree bank

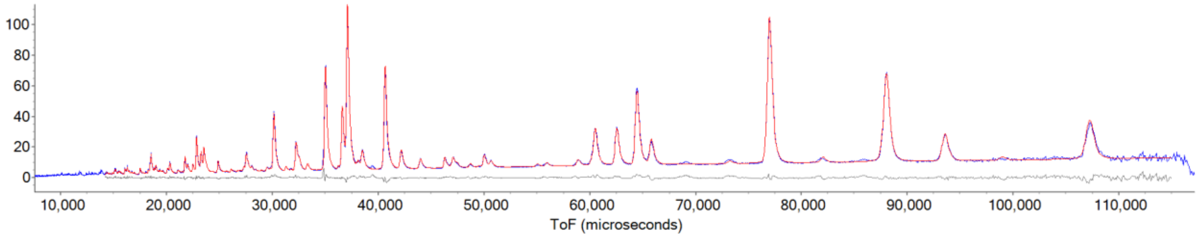
sample A 55 K / 90 degree bank

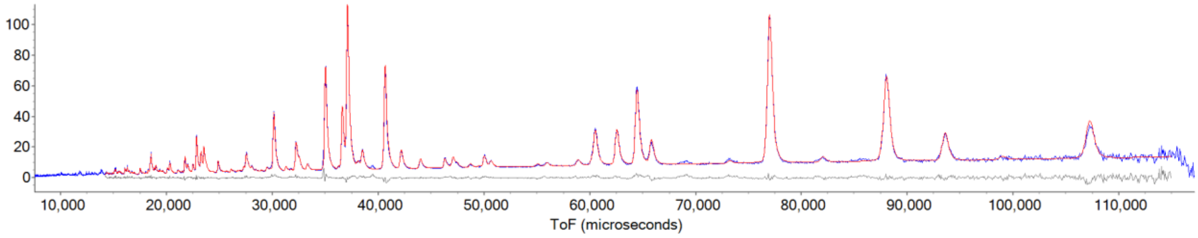
sample A 65 K / 90 degree bank

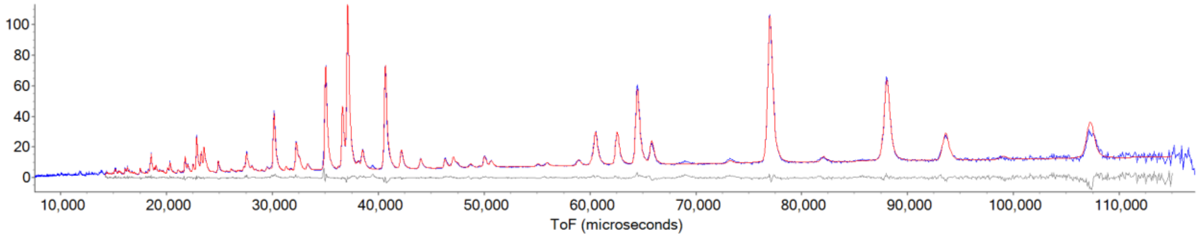
sample A 75 K / 90 degree bank

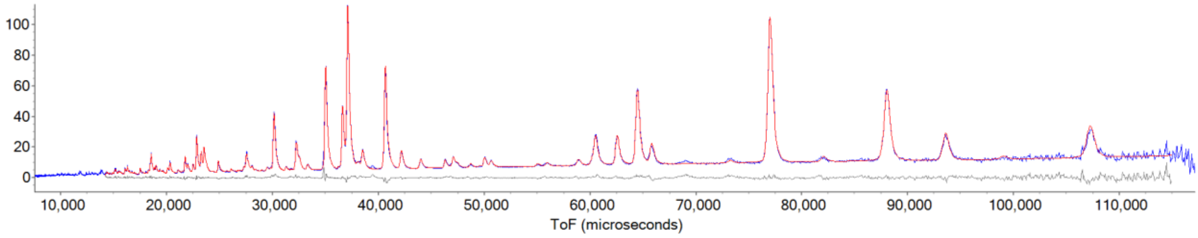
sample A 85 K / 90 degree bank

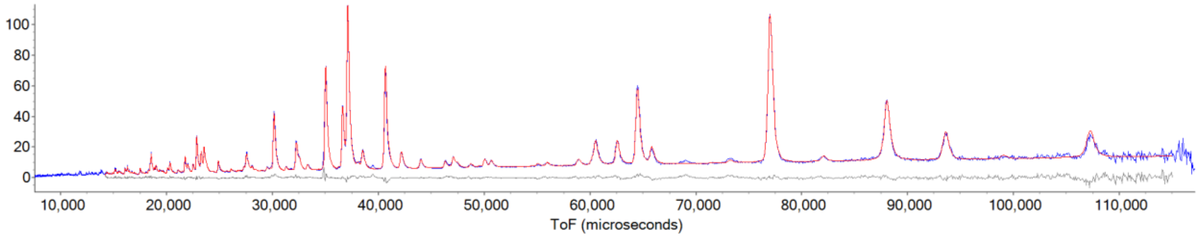
sample A 90 K / 90 degree bank

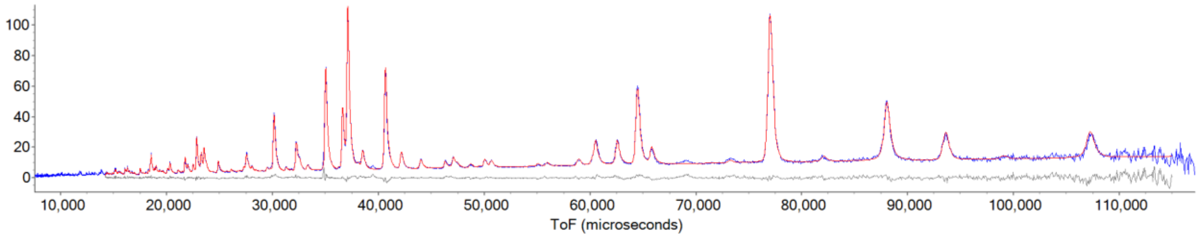
sample A 91 K / 90 degree bank

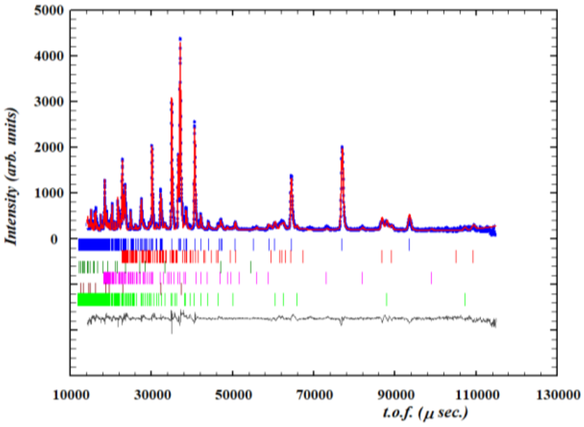
Sample A 92K / 90 degree bank

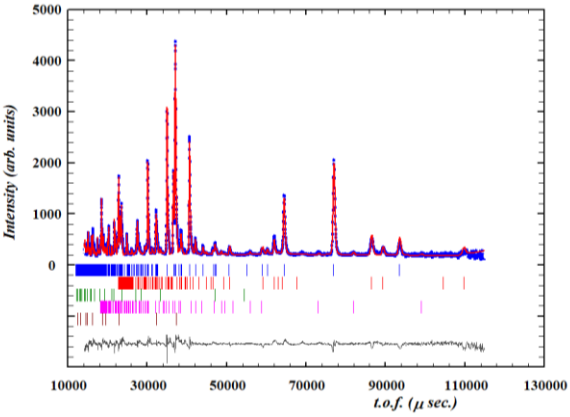
Sample A 93 K / 90 degree bank

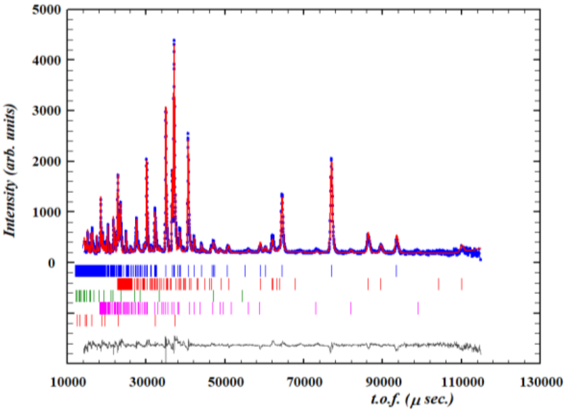
Sample A 94 K / 90 degree bank

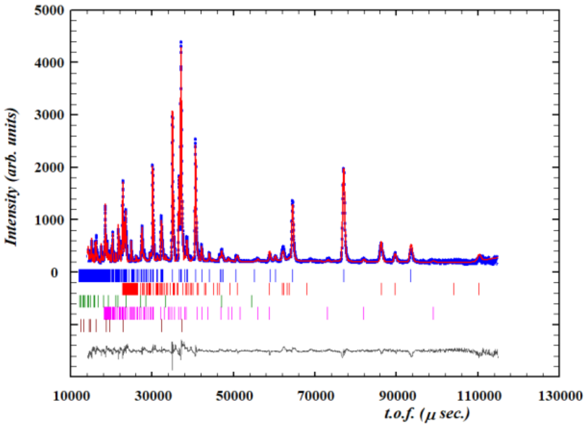
Sample A 95 K / 90 degee bank

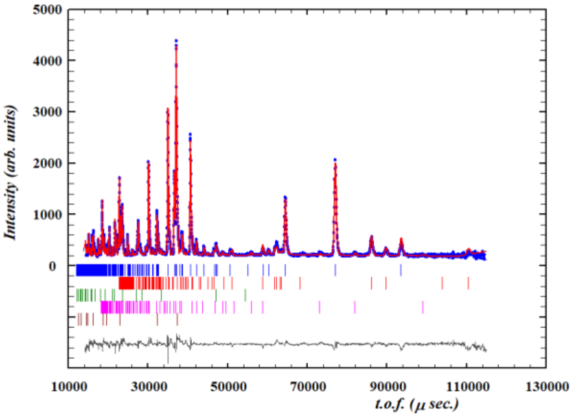
Sample A 96K / 90 degree bank

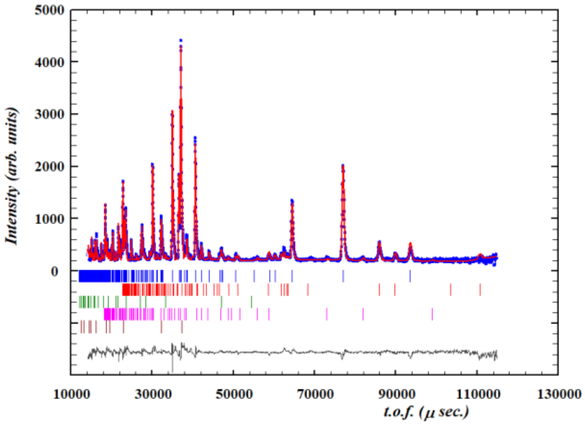
Sample A 98 K / 90 degree bank

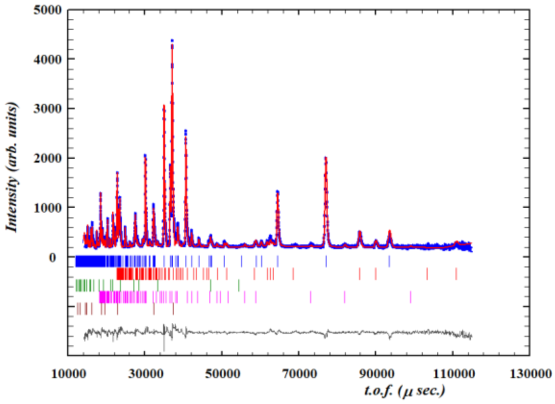
Sample A 100 K / 90 degree bank

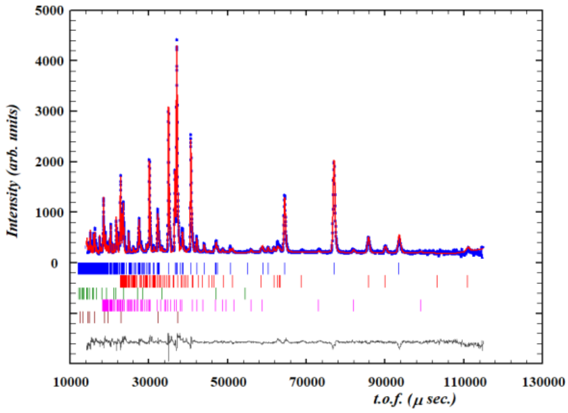
Sample A 102 K / 90 degree bank

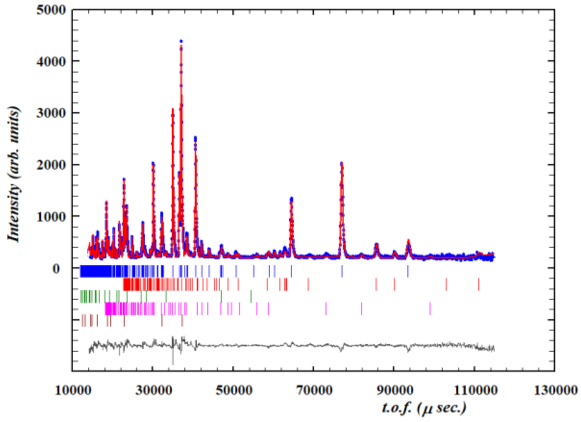
Sample A 105 K / 90 degree bank

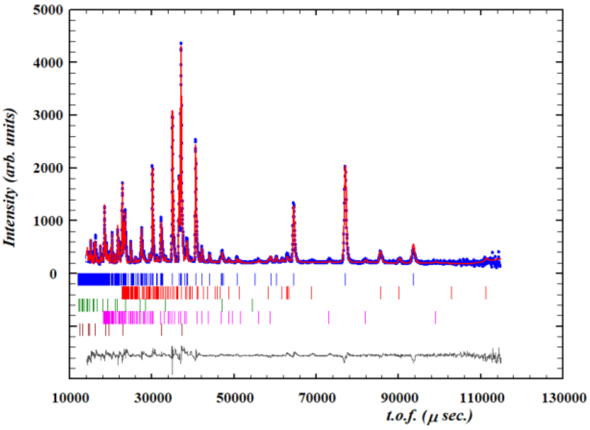
Sample A 108 K / 90 degee bank

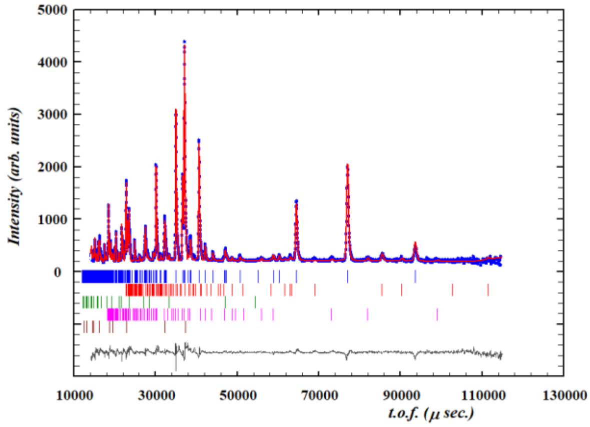
Sample A 113 K / 90 degee bank

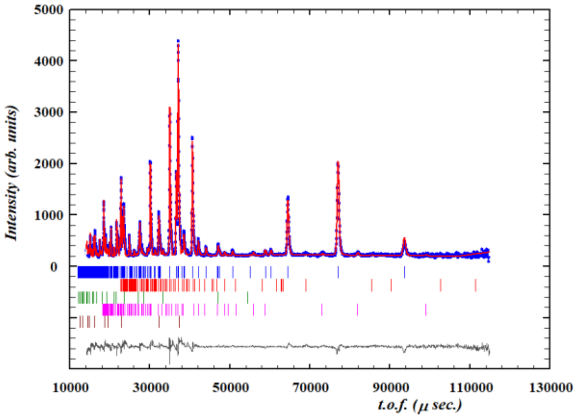
Sample A 119 K / 90 degee bank

sample A 125 K / 90 degree bank

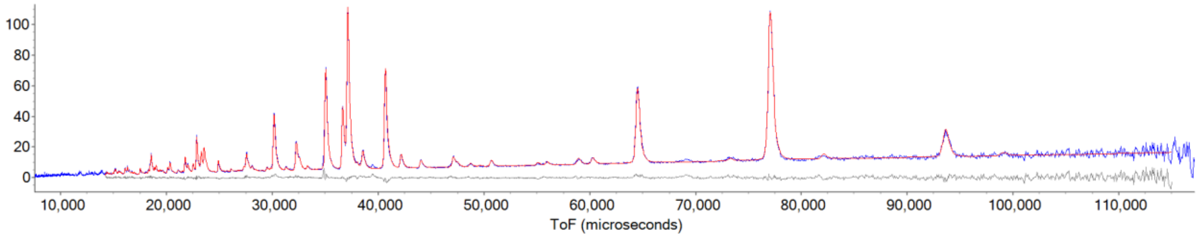

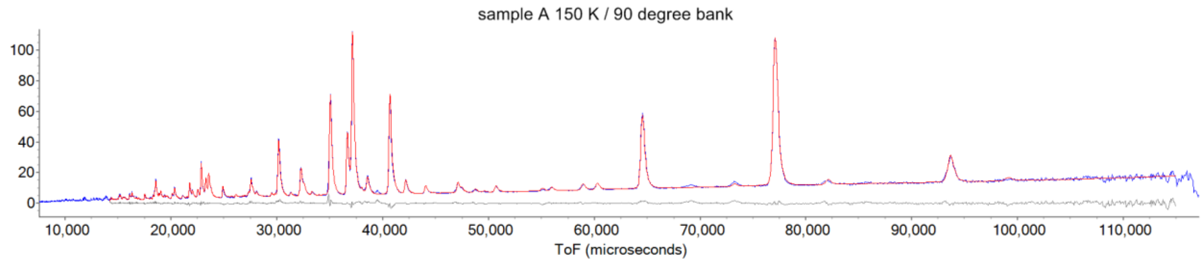
sample A 150 K / 90 degree bank

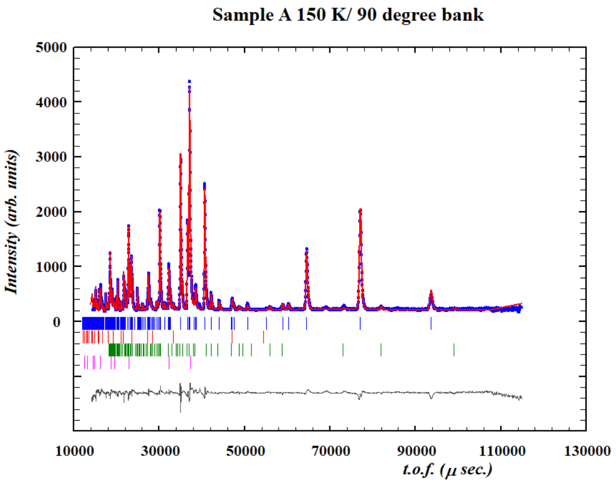
Sample A 150 K/ 90 degree bank

Figure S7. Rietveld refinements for sample B (20, 55, and 97 K patterns are from the same refinements as in Figures 10, 6, and 9 in the main paper, respectively). See also Table 1 in the main text.

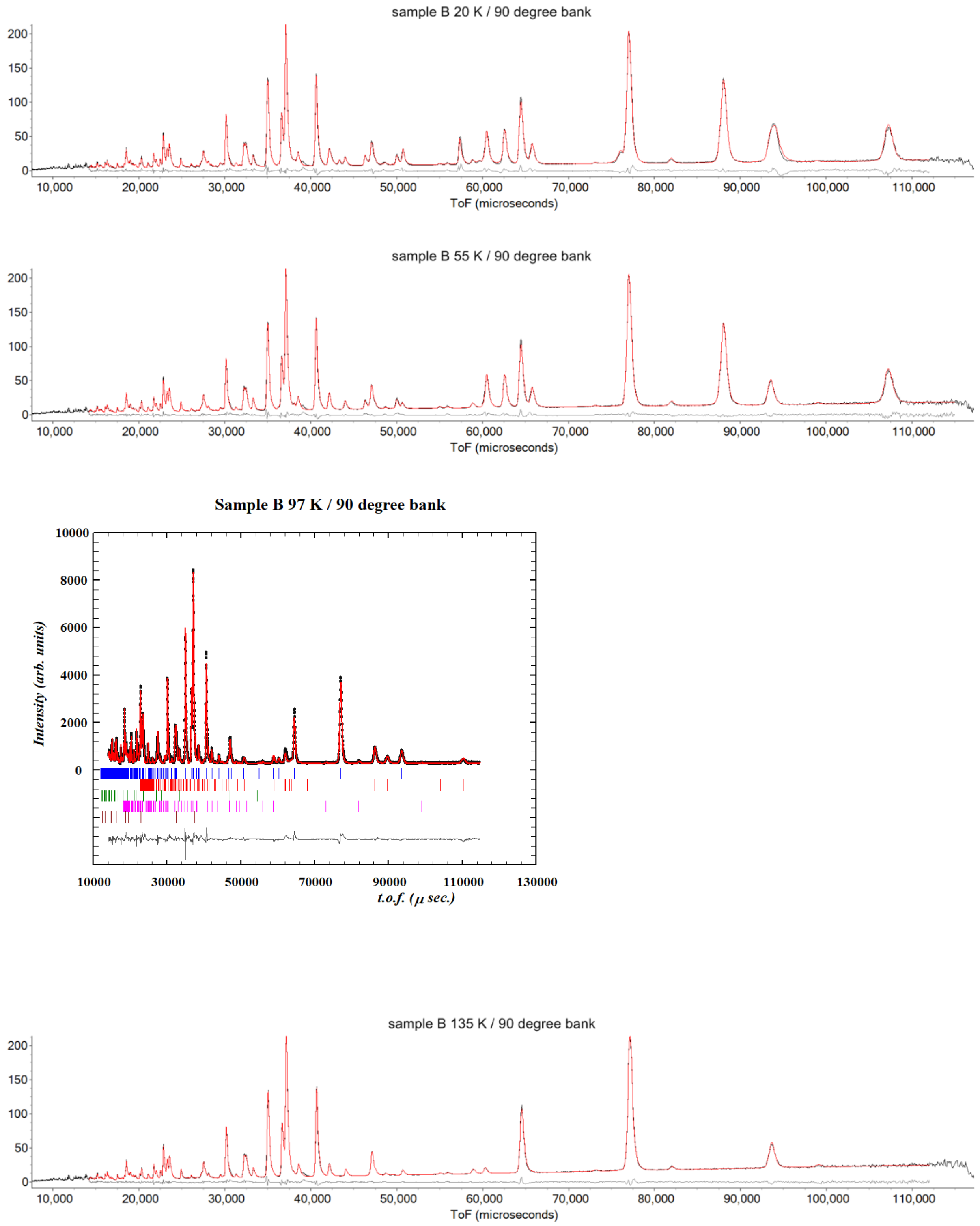

Table S7. Agreement factors for modelling of the neutron diffraction data of sample A

Temperature (K)	Rwp_bank1	Rwp_bank2	Rwp_bank3	Rwp_bank4	Rwp_bank5	Rwp_global	Refinement software
1.5	2.776	3.733	4.513	4.929	5.345	4.21	Topas Academic
20	4.141	4.639	4.855	5.397	5.529	4.88	Topas Academic
30	4.36	4.549	4.86	5.48	5.534	4.91	Topas Academic
36	4.097	4.658	4.75	5.347	5.497	4.85	Topas Academic
42	3.852	4.481	4.738	5.292	5.395	4.73	Topas Academic
45	3.815	4.324	4.711	5.338	5.419	4.68	Topas Academic
48	3.798	4.062	4.309	5.099	5.256	4.45	Topas Academic
51	3.913	4.243	4.341	5.121	5.208	4.53	Topas Academic
55	2.625	3.601	4.149	4.867	5.199	4.04	Topas Academic
65	3.758	4.083	4.455	5.171	5.304	4.50	Topas Academic
75	3.675	4.107	4.495	5.196	5.31	4.51	Topas Academic
85	3.681	4.251	4.467	5.164	5.385	4.55	Topas Academic
90	3.883	4.281	4.555	5.22	5.379	4.62	Topas Academic
91	4.496	4.697	4.782	5.348	5.262	4.89	Topas Academic
92	19.4	11.7	11.5	11.8	12.5	13.0	FullProf
93	19.7	12.1	11.6	12	12.4	13.2	FullProf
94	20	14.3	15.6	16.8	17.7	16.4	FullProf
95	18.5	11.8	11.6	11.9	12.5	12.9	FullProf
96	19.2	11.9	11.4	11.7	12.5	13.0	FullProf
98	18.8	11.6	11.5	11.7	12.5	12.8	FullProf
100	18.1	11.5	11.4	11.7	12.4	12.7	FullProf
102	18.9	11.4	11.5	11.8	12.4	12.8	FullProf
105	18.9	11.2	11.5	11.7	12.3	12.7	FullProf
108	19.7	11.2	11.3	11.7	12.3	12.8	FullProf
113	19.3	11	11.2	11.7	12.3	12.6	FullProf
119	19.7	10.8	11.3	11.6	12.2	12.6	FullProf
125	4.453	4.371	4.687	5.204	5.242	4.74	Topas Academic
135	3.588	3.98	4.4	5.04	5.13	4.38	Topas Academic
150	2.291	3.079	3.972	4.661	5.013	3.73	Topas Academic
150	14.2	10.5	11.1	11.5	12.1	11.6	FullProf

Figure S8. The cycloidal fits to PND data at 96 K show clear discrepancies with the experimental intensity in contrast with the incommensurate spin-density wave model shown in Figure 9 of the main text. Upper blue tickmarks: nuclear structure; lower red tickmarks: magnetic structure.

ab plane cycloidal model

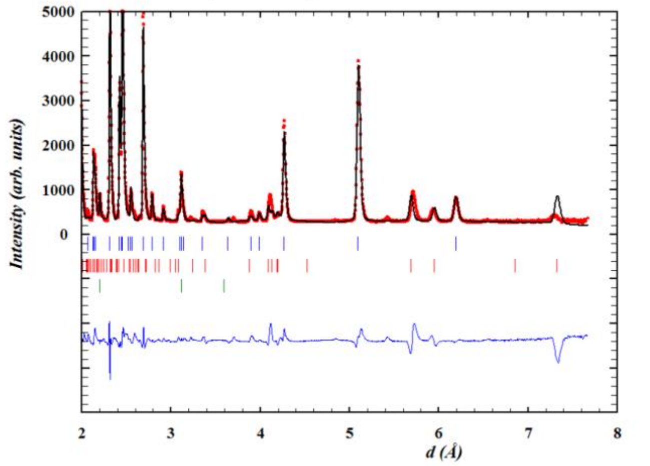

ac plane cycloidal model

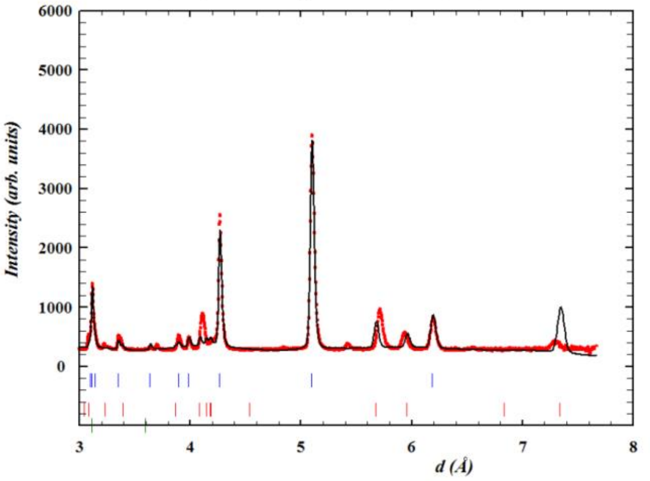

bc plane cycloidal model